bioRxiv preprint doi: https://doi.org/10.1101/791368; this version posted October 2, 2019. The copyright holder for this preprint (which was not certified by peer review) is the author/funder. All rights reserved. No reuse allowed without permission.

ATP-driven separation of liquid phase condensates in bacteria

B. Guilhas[1], J.C. Walter[2], J. Rech[3], G. David[2], N.-O. Walliser[2], J. Palmeri[2], C., Mathieu-Demaziere[3], A. Parmeggiani[2,4], J.Y. Bouet[3], A. Le Gall[1], M. Nollmann[1#]

[1] Centre de Biochimie Structurale, CNRS UMR 5048, INSERM U1054, Université de Montpellier, 60 rue de Navacelles, 34090, Montpellier, France

[2] Laboratoire Charles Coulomb (L2C), Univ. Montpellier, CNRS, Montpellier, France.

[3] LMGM, CBI, CNRS, Univ. Toulouse, UPS, Toulouse, France.

[4] LPHI, CNRS, Univ. Montpellier, Montpellier, France.

 # Corresponding author

bioRxiv preprint doi: https://doi.org/10.1101/791368; this version posted October 2, 2019. The copyright holder for this preprint (which was not certified by peer review) is the author/funder. All rights reserved. No reuse allowed without permission.

Abstract

Liquid-liquid phase separated (LLPS) states are key to compartmentalise components in the absence of membranes, however it is unclear whether LLPS condensates are actively and specifically organized in the sub-cellular space and by which mechanisms. Here, we address this question by focusing on the ParAB*S* DNA segregation system, composed of a centromeric-like sequence (*parS*), a DNA-binding protein (ParB) and a motor (ParA). We show that *parS*-ParB associate to form nanometer-sized, spherical droplets. ParB molecules diffuse rapidly within the nucleoid volume, but display confined motions when trapped inside ParB droplets. Single ParB molecules are able to rapidly diffuse between different droplets, and droplet nucleation is strongly favoured by *parS*. Notably, the ParA motor is required to prevent the fusion of ParB droplets. These results describe a novel active mechanism that splits, segregates and localises LLPS condensates in the sub-cellular space.

Keywords

liquid droplets; phase separation; liquid phase-condensation; plasmid partition; ParABS; single particle tracking, photo-activated localization microscopy.

bioRxiv preprint doi: https://doi.org/10.1101/791368; this version posted October 2, 2019. The copyright holder for this preprint (which was not certified by peer review) is the author/funder. All rights reserved. No reuse allowed without permission.

Introduction

In the past, bacteria were often viewed as homogeneous systems lacking the complex sub-cellular spatial organization patterns observed in eukaryotes. The advent of powerful labeling and imaging methods has enabled the discovery of a plethora of mechanisms used by bacteria to specifically and precisely localize components, in space and time, within its sub-cellular volume (Shapiro et al., 2009; Surovtsev and Jacobs-Wagner, 2018). These mechanisms include pole-to-pole oscillatory systems to define the site of cell division (e.g. MinCDE), dynamic, ATP-driven polymerization to drive cell division and cell growth (e.g FtsZ, MreB), recognition of cell curvature to localize chemotaxis complexes (e.g. DivIVA, (Ramamurthi and Losick, 2009)), ATP-powered translocation of membrane-bound machines to power cell motility (e.g. Agl-Glt (Faure et al., 2016)), or nucleoid-bound oscillatory systems to localize chromosomal loci (e.g. ParABS, (Le Gall et al., 2016)). More recently, it became apparent that many cellular components (e.g. ribosomes, RNA polymerases, P-granules) (van Gijtenbeek et al., 2016; Moffitt et al., 2016; Racki et al., 2017; Sanamrad et al., 2014) display specific sub-cellular localization patterns, leading to the spatial segregation of biochemical reactions (e.g. translation, transcription, or polyP biosynthesis). Most notably, bacteria are able to achieve this precise sub-cellular compartmentalization without resorting to membrane-enclosed organelles.

Recently, important progress has been made in understanding the formation of membrane-less organelles in eukaryotic cells (Hyman et al., 2014). A combination of *in vitro* and *in vivo* experiments demonstrated that such compartments are formed by liquid-liquid phase separation (LLPS), a mechanism similar to liquid demixing (Hyman et al., 2014). It consists of a thermodynamic process through which attractive molecular interactions counterbalance entropy-driven effects. This phenomenon promotes the self-organisation of

bioRxiv preprint doi: https://doi.org/10.1101/791368; this version posted October 2, 2019. The copyright holder for this preprint (which was not certified by peer review) is the author/funder. All rights reserved. No reuse allowed without permission.

a condensed phase, in which molecules are close enough from each other to experience their mutual attraction, interfaced with a dilute phase. This mechanism provides advantages such as rapid assembly/disassembly, absence of a breakable membrane, and has been shown to serve fundamental biological processes such as regulation of biochemical reactions, sequestration of toxic factors, or to play the roles of organisation hubs (Shin and Brangwynne, 2017).

The first evidence that eukaryotic cells use LLPS came from examination of P granules in *C. elegans* (Brangwynne et al., 2009). In this study, Brangwynne et al. observed different key signatures of liquid droplets: P granules formed spherical bodies that could fuse together, drip and wet, and with a dynamic internal organisation. Since then, many other processes have been shown to display LLPS properties (Banani et al., 2017). More recently, it was discovered that bacterial ribonucleoprotein granules assemble into LLPS droplets (Al-Husini et al., 2018) and that the bacterial cell division protein FtsZ forms condensates when in complex with SlmA (Monterroso et al., 2019). Thus, although LLPS seems to be a universal mechanism to compartmentalise components in the absence of membranes, it is unclear whether LLPS condensates are actively and specifically organized in the sub-cellular space and by which mechanisms.

We addressed this problem by investigating how specific DNA sequences are organized within the sub-cellular volume in space and time. We focused on the ParABS partition system, responsible for chromosome and plasmid segregation in bacteria and archaea (Baxter and Funnell, 2014; Bouet et al., 2014; Schumacher et al., 2015; Toro and Shapiro, 2010). This system is composed of three components: (1) a centromeric sequence (*parS*); (2) a dimeric DNA binding protein (ParB) that binds *parS;* and (3) a Walker A ATPase (ParA). We have previously shown that ParB is very abundant (>850 dimers per cell) (Bouet

bioRxiv preprint doi: https://doi.org/10.1101/791368; this version posted October 2, 2019. The copyright holder for this preprint (which was not certified by peer review) is the author/funder. All rights reserved. No reuse allowed without permission.

et al., 2005), localizes to a large extent (~90% of ParB molecules) to regions containing *parS* (Sanchez et al., 2015) to form a tight nucleoprotein complex (partition complex). Formation of the partition complex requires weak ParB-ParB dimer interactions mediated by its disordered, low-complexity region. Here, we used super-resolution microscopy and single-particle analysis to investigate the physical mechanisms involved in the formation of partition complexes. We show that partition complexes are small (<50nm), spherical objects. Single, isolated ParB molecules diffuse rapidly within the nucleoid volume, but display confined motions when trapped inside partition complexes. These results suggest a partition of ParB into two phases: a gas-like phase, and a dense, liquid-like condensate phase that shows nanometer-sized, spherical droplets. Next, we show that the nucleation of ParB condensates is strongly favoured by the presence of the centromeric sequence *parS*. Separation and proper sub-cellular localization of ParB condensates require the ParA motor. Critically, different ParB condensates collapse into a single droplet upon the degradation of ParA. These results describe a novel active mechanism that splits, segregates and localises LLPS condensates in the sub-cellular space.

Results

ParB assembles into spherical nano-condensates

Previous studies have revealed that the partition complex is made of ~300 dimers of ParB (Adachi et al., 2006; Bouet et al., 2005) and ~10kb of *parS*-proximal DNA (Rodionov et al., 1999). This complex is held together by specific, high-affinity interactions between ParB and *parS*, and by low-affinity interactions between ParB dimers that are essential for the power-law distribution of ParB around *parS* sites (Figure 1A) (Debaugny et al., 2018; Sanchez

bioRxiv preprint doi: https://doi.org/10.1101/791368; this version posted October 2, 2019. The copyright holder for this preprint (which was not certified by peer review) is the author/funder. All rights reserved. No reuse allowed without permission.

et al., 2015). However, technological limitations have thwarted the investigation of the physical mechanisms involved in the formation of partition complexes.

We addressed these limitations by first investigating the shape and size of the partition complex, reasoning that the former should inform us on the role of the mechanisms involved in the maintenance of the complex cohesion while the latter would enable an estimation of protein concentration within the partition complex. To this aim, we combined Photo-Activated Localisation Microscopy (PALM) (Fiche et al., 2013; Marbouty et al., 2015) with single-particle reconstruction (Salas et al., 2017), and used a previously validated functional ParB-mEos2 fusion strain (Sanchez et al., 2015). In addition, we implemented an efficient and well-controlled fixation protocol (Figure S1A and Methods) to limit the influence of partition complex dynamics and reach a localization precision of $14 \pm 6\ nm$ (Figures S1B-C). Most single ParB particles localized to the partition complex, as we previously observed by live PALM (Sanchez et al., 2015) (Figure 1B). Next, we clustered localizations pertaining to each partition complex using a density-based clusterization algorithm (Cattoni et al., 2017; Levet et al., 2015). Partition complexes were positioned near the quarter cell positions (Figure S1A), as reported previously (Le Gall et al., 2016). Partition complex shapes displayed heterogeneity, reflecting the different three dimensional projections and conformational states of the complex (Figure 1B-C). Thus, we used single-particle analysis to classify them into eight major class averages that contained most partition complexes (Figure 1C, S1D-E) and to generate 3D reconstructions with isotropic resolution (Figure 1D) (Salas et al., 2017).

Next, we estimated the size of the partition complex by calculating the mean full width at half maximum of the reconstructions obtained from each single class average (43 $\pm$ 7 nm) (Figure S1F). Thus, from the size of the partition complex and the average number of

bioRxiv preprint doi: https://doi.org/10.1101/791368; this version posted October 2, 2019. The copyright holder for this preprint (which was not certified by peer review) is the author/funder. All rights reserved. No reuse allowed without permission.

ParB in each partition complex (~300 ParB dimers) (Adachi et al., 2006; Bouet et al., 2005), we can estimate a local ParB dimer concentration of the order of ~10 mM. Remarkably, this extremely high concentration is comparable to that of the total protein concentration in the bacterial cytoplasm (~10 mM, for proteins of the same size as ParB) (Elowitz et al., 1999), suggesting that ParB dimers represent most of the total protein volume within a partition complex. ParB dimers interact together with sub-µM affinities (0.3-1 µM) (Sanchez et al., 2015; Taylor et al., 2015), thus we expect virtually every ParB dimer within a partition complex to be interacting with another ParB dimer. Finally, these estimations predict a mean intermolecular distance between ParB dimers of ~3 nm, comparable to the size of a ParB dimer itself (~3 nm, assuming its interaction volume to be a sphere) (Schumacher and Funnell, 2005). Overall, these data suggest that partition complexes share many of the properties of liquid-like condensed phases.

ParB exists in an equilibrium between liquid- and gas-like phases

Next, we investigated whether single ParB dimers were able to escape partition complexes and at what frequencies by using single-particle tracking PALM (sptPALM) (Le Gall et al., 2016; Sanchez et al., 2015). We observed two distinct dynamic behaviors reflected by static (or confined) and mobile trajectories (Figure 2A) with clearly different apparent diffusional properties (Figure 2B). Previous studies reported similar apparent diffusion coefficients for immobile and freely-diffusing DNA-binding proteins (Stracy et al., 2015). Interestingly, most ParB particles were static (~95%), and only a small proportion of particles were dynamic (<5%) (Figure 2B).

Static trajectories localized near the quarter cell positions, similarly to ParB complexes (Figure S2A). To determine whether these trajectories clustered in space, we

bioRxiv preprint doi: https://doi.org/10.1101/791368; this version posted October 2, 2019. The copyright holder for this preprint (which was not certified by peer review) is the author/funder. All rights reserved. No reuse allowed without permission.

calculated the pair correlation between static trajectories (see Methods). For a homogeneous distribution we would expect a flat line (see dashed curve in Figure 2C). In contrast, we observed a sharp peak at short distances, indicating that static ParB particles are spatially confined within partition complexes (Figure 2C, blue curve). Mobile trajectories, instead, occupied the whole nucleoplasmic space (Figure S2A). Thus, from the percentage of mobile trajectories detected (~5% of all trajectories), and the estimated number of ParB dimers per cell (~800), one can estimate that only ~20 ParB dimers are typically moving between ParB droplets. Mobile ParB dimers move on the nucleoplasmic volume, thus we estimate that this species exists at a concentration of ~20 nM, five orders of magnitude smaller than the ParB concentration within partition complexes (~10 mM). Therefore, these results suggest that ParB molecules exist in two well-defined phases: a highly condensed, liquid-like state (ParB condensate) and a diluted gas-like phase.

ParB diffuses across phase boundaries

This interpretation suggests that single ParB molecules should be able to diffuse between two different partition complexes within the same cell. To test this, we photobleached a single partition complex and monitored the total fluorescence signal in both the bleached and unbleached complex (Figure 2D). Strikingly, we observed a clear increase in the fluorescence signal of the bleached complex over time with a concomitant decrease of the fluorescence signal of the unbleached complex (Figures 2D-E). This behaviour can only be explained by the influx of fluorescent proteins into the bleached complex and by their escape from the unbleached complex. The symmetry between both curves suggests that both fluxes have similar magnitudes (Figure 2E, S2B). By modeling the diffusion process, we could fit the experimental curves to a model and estimated the

bioRxiv preprint doi: https://doi.org/10.1101/791368; this version posted October 2, 2019. The copyright holder for this preprint (which was not certified by peer review) is the author/funder. All rights reserved. No reuse allowed without permission.

residence time of a ParB molecule in a ParB condensate to be ~ 100 s (Figures S2C-E), while the typical time in the gas-like phase was ~23 s. Note that these typical times provide a good estimate (~90%) of the number of ParB dimers confined within partition complexes (see Figure S2).

Eventually, the system reached equilibrium (after ~4 min). At this point, the fluorescence intensities of bleached and unbleached complexes became equal, indicating that ParB molecules equipartitioned between the two condensates. Notably, this equipartition suggests that these droplet-like condensates are in mutual stationary equilibrium at times smaller than the cell cycle. This is contrary to the intuition one would have for classical droplet systems (see e.g. Ostwald ripening, (Hyman et al., 2014)) in a small and confined environment. We note that a dynamic exchange of ParB dimers between ParB condensates would only be possible if single ParB dimers were diffusing across the liquid-like and gas-like phase boundaries, therefore equilibrating chemical potentials between these two phases (Hyman et al., 2014).

ParB condensates are able to merge

Biomolecular condensates can exhibit different internal architectures. For example, the Balbiani body is a solid-like structure held together by a matrix of amyloid-like fibers (Shin and Brangwynne, 2017), while liquid-like behavior of P granules denotes an internal disordered organization. Thus, the ability of two compartments to fuse helps distinguish between these two different internal structures. To study whether ParB condensates were able to fuse over time, we performed live time-lapse fluorescence microscopy experiments. At short time scales (~secs), we observed that independent partition complexes were able to fuse into a single, stable partition complex (Figure 2F). Notably, we observed that fused

bioRxiv preprint doi: https://doi.org/10.1101/791368; this version posted October 2, 2019. The copyright holder for this preprint (which was not certified by peer review) is the author/funder. All rights reserved. No reuse allowed without permission.

complexes move in concert during several seconds (Figure 2F). We note that this ability of ParB complexes to fuse is not unique to the F-plasmid system, and was also observed for P1 plasmids which also segregate using a ParABS system (Sengupta et al., 2010). Altogether, these results suggest that ParB partition complexes possess key signatures of liquid-like droplets.

***ParS,* and low- and high-affinity ParB interactions are sufficient for phase separation**

Next, we performed a thermodynamic analysis and Monte-Carlo simulations to find the minimal set of assumptions that would be necessary to reproduce an equilibrium between liquid- and gas-like phases. For this, we considered a minimalistic gas-liquid lattice model that shows in mean field theory a generic LLPS diagram (Figure S3A). For the Monte-Carlo simulations, three hundred ParB particles were generated on a three-dimensional 2x0.5x0.5 μm^3 lattice with a spacing of 5 nm. The F-plasmid was represented by a single, static, high affinity binding site within this lattice containing a repeat of 10 *parS* sequences (similar to the natural F-plasmid). ParB interacted with high affinity with the *parS* cluster (hereafter *parS10*), with low-affinity to other sites in the lattice, and with low-affinity with itself. Affinities and concentrations were based on experimentally-determined coefficients (Figure S3). The system was left to evolve under different initial conditions (pure gas-like or liquid-like states) and in the presence or absence of *parS10*. The system remained in a gas-like phase in the absence of *parS10* (Figure 3A, green curve). In contrast, in the presence of *parS10* the system displayed several transitions that involved *parS* binding, nucleation, and stable co-existence of liquid- and gas-like phases (Figure 3A, blue curve). The system evolved towards the same endpoint when the initial condition was a pure liquid-like state (Figure 3A, gray curve). At this endpoint, 80% of the

bioRxiv preprint doi: https://doi.org/10.1101/791368; this version posted October 2, 2019. The copyright holder for this preprint (which was not certified by peer review) is the author/funder. All rights reserved. No reuse allowed without permission.

molecules were in a liquid-phase and the remainder in a gas-like state, mirroring the proportions observed experimentally (Figure 2B). These results suggest that the only required elements to reach a stable coexistence between liquid and gas-like ParB phases are: low-affinity interactions between ParB dimers and non-specific DNA, and high-affinity interactions between ParB and the nucleation sequence *parS*. Critically, ParB was unable to form a stable liquid-gas coexistence phase in the absence of *parS* within physiological timescales (Figure 3A, green curve).

We experimentally tested this observation by performing sptPALM experiments in a strain lacking *parS*. In contrast to our previous results, we frequently observed mobile trajectories (Figure 3B-C). In fact, the proportion of this population increased from ~5% in the wild-type to ~50% in the absence of *parS*. The persistence of such a large proportion of static trajectories could suggest that ParB is still able to assemble into liquid-like phases, but now in transient or instable condensates. To investigate this possibility, we performed pair-correlation analysis of static trajectories (Figure 3D). Clearly, static trajectories clustered together in the presence of *parS* (dashed curve), but were rather homogeneously distributed in the absence of *parS* (green curve). These observations are consistent with previous reports showing that ParB foci are not detectable in the absence of *parS* (Erdmann et al., 1999) or with *parS*-binding deficient ParB (Sanchez et al., 2013). Overall, these data fully agree with our simulations and indicate that the centromeric sequence *parS* is essential for the assembly of stable liquid-like ParB condensates.

Motor proteins drive ParB condensates out-of-equilibrium

At equilibrium, a passive system undergoing phase separation displays a single condensed phase: if initially multiple condensed phases are found, the lowest energy state

bioRxiv preprint doi: https://doi.org/10.1101/791368; this version posted October 2, 2019. The copyright holder for this preprint (which was not certified by peer review) is the author/funder. All rights reserved. No reuse allowed without permission.

comprises a single liquid-separated phase that can be reached either by fusion or through Ostwald ripening (Zwicker et al., 2014). Partition systems have specifically evolved to ensure faithful DNA segregation to daughter cells, which would be impeded by fusion into single, stable partition complexes. Our previous time-lapse fluorescence microscopy experiments showed that single partition complexes can merge at short time-scales (tens of seconds, Figure 2F). At longer time-scales (tens of minutes), however, ParB condensates are not only kept apart from each other but are also actively segregated concomitantly with the growth of the host cell (Figure 4A). Previous reports have shown that the ParA motor protein is necessary to ensure faithful separation and segregation of partition complexes (Erdmann et al., 1999; Le Gall et al., 2016). This function requires both ParA's ATP hydrolysis activity and its stimulation by ParB (Ah-Seng et al., 2013; Le Gall et al., 2016), and would ensure ParB droplet segregation. However, it is not clear whether ParA may play a role at preventing fusion of ParB droplets.

If ParA was the factor preventing fusion of ParB condensates, then its slow removal should lead to the fusion of all ParB condensates in a cell. To test this hypothesis, we generated a strain where ParA can be selectively degraded using a degron system (McGinness et al., 2006) (Figure 4B). In this strain, we observed the almost complete disappearance of ParA after 30 min of degron induction (Figure 4C). In the absence of ParA degradation, this strain displayed typical ParB condensate separation dynamics (Figure 4D, white traces). Strikingly, we observe the fusion of ParB condensates upon degradation of ParA (Figure 4E, white traces). Over time, the number of ParB condensates per cell collapses to 0.6 ± 0.7 ParB condensates/cell when ParA is degraded, but remains at 2.9 ± 1.0 ParB condensates/cell in the presence of ParA (Figure 4F). Overall, these data indicate that the

bioRxiv preprint doi: https://doi.org/10.1101/791368; this version posted October 2, 2019. The copyright holder for this preprint (which was not certified by peer review) is the author/funder. All rights reserved. No reuse allowed without permission.

action of the ParA motor is required to keep ParB condensates out of equilibrium by preventing their fusion.

Discussion

Here, we provide evidence in support of a new class of droplet-like-forming system with unique properties that ensure the stable coexistence and regulated inheritance of separate liquid-condensates. Interestingly, the three components of the ParABS partition system and the exquisite regulation of their multivalent interactions are required to observe this complex behavior: (1) High-affinity interactions of ParB and the *parS* centromeric sequence are necessary for the nucleation of the ParB condensate; (2) Weak interactions of ParB with chromosomal DNA and with itself are necessary to produce phase separation; (3) Finally, the ParA ATPase is required to counter droplet fusion and generate segregation.

In passive phase-separation systems, separate liquid droplets grow by taking up material from a supersaturated environment, by Ostwald ripening, or by fusion of droplets. Over time, these processes lead to a decrease in the number of droplets and an increase in their size. This reflects the behaviour we observed for ParB condensates upon depletion of the ParA ATPase. Recently, theoretical models have predicted mechanisms to enable the stable coexistence of multiple liquid phases (Zwicker et al., 2015). These mechanisms require constituents of the phase separating liquids to be converted into each other by nonequilibrium chemical reactions (Zwicker et al., 2015, 2016). Our result that ParA is required to maintain ParB condensates well separated indicates the existence of an alternative and novel mechanism to actively control the number and size of droplets within cells, as well as their fission. Interestingly, similar mechanisms –yet to be discovered– could control the number, size, and sub-cellular localization of other droplet-forming systems such

bioRxiv preprint doi: https://doi.org/10.1101/791368; this version posted October 2, 2019. The copyright holder for this preprint (which was not certified by peer review) is the author/funder. All rights reserved. No reuse allowed without permission.

as P-granules (Brangwynne, 2011), stress granules (Jain et al., 2016), or heterochromatin domains (Strom et al., 2017).

Acknowledgments

This project has received funding from the European Research Council (ERC) under the European Union's Horizon 2020 Research and Innovation Program (Grant ID 724429) (M.N.), the Agence Nationale pour la Recherche grant HiResBacs (ANR-15-CE11-0023) (M.N.) and grant IBM (ANR-14-CE09-0025-01) (M.N., J-Y.B, A.P.), the Program 'Investissements d'Avenir' for the Labex NUMEV (2011-LABX-076) integrated into the I-Site MUSE (AAP 2013-2-005, 2015-2-055, 2016-1-024) (G.D., J-C.W., N-O.W., J.P., A.P.) and the CNRS INPHYNITI program (J-C.W.). We acknowledge the France-BioImaging infrastructure supported by the French National Research Agency (grant ID ANR-10-INBS-04, ''Investments for the Future''). B.G. and G.D. were supported by a PhD fellowship from the French Ministère de l'Enseignement Supérieur, de la Recherche et de l'Innovation.

Data availability statement

The data that support the findings of this study are available from the corresponding author upon reasonable request.

Code availability

Most analysis tools and methods used in this study are in the open domain (see Methods). Code developed specifically for this manuscript can be obtained from the corresponding author upon request.

bioRxiv preprint doi: https://doi.org/10.1101/791368; this version posted October 2, 2019. The copyright holder for this preprint (which was not certified by peer review) is the author/funder. All rights reserved. No reuse allowed without permission.

Methods

Sample preparation

sptPALM, PALM, FRAP and time-lapse microscopy (fast dynamics)

Microscopy coverslips and glass slides were rinsed with acetone and sonicated in a 1M KOH solution for 20 minutes. Next, they were dried over an open flame to eliminate any remaining fluorescent contamination. A frame of double-sided adhesive tape was placed on a glass slide and a ~5mm channel was extruded from its center. 20 µl of 2 % melted agarose (diluted in M9 media, melted at 80°C; for the imaging of DLT3469 strain: 1 % melted agarose diluted in M9 + 0.2% arabinose) were spread on the center of the glass slide and covered with a second glass slide to ensure a flat agarose surface. The sandwich slides were kept on a horizontal position for 5 min under external pressure at room temperature (RT) to allow the agarose to solidify. The top slide was then carefully removed when bacteria were ready to be deposited in the agar pad (see below). Cells were harvested during the exponential phase (optical density at 600 nm: ~0.3). For PALM experiments, cells were fixed in a 2% PFA solution for 15 min at room temperature and 30 min at 4°C (for the detailed procedure, refer to (Visser et al., 2017)). A bacterial aliquot was spun down in a bench centrifuge at RT at 3000g for 3 minutes. The supernatant was then discarded and the pellet re-suspended in 10 µl of minimal media. 1.5 µl of 1/10 fiducial beads (TetraSpeck TM, Life Technologies) were added. 1.7 µl of the resulting bacterial solution were pipetted onto the agar. After deposition of bacteria, the second face of the double-sided tape was removed and the pad was then sealed with a clean coverslip.

bioRxiv preprint doi: https://doi.org/10.1101/791368; this version posted October 2, 2019. The copyright holder for this preprint (which was not certified by peer review) is the author/funder. All rights reserved. No reuse allowed without permission.

Time-lapse microscopy (slow dynamics)

Long-term ParB-GFP droplet dynamics (Figure 4) were monitored by following the movement of ParB droplets over several cell cycle times. For this, cells were first harvested during the exponential phase (optical density at 600 nm: ~0.3), then diluted to 1:300 to adjust the bacterial density on the field of view, and finally deposed in an ONIX CellAsic microfluidic chamber (B04A plates; Merck-Millipore). Bacteria were immobilized and fresh culture medium (supplemented with 0.2% arabinose) was provided (10.3 kPa) throughout the acquisition.

Fluorescence microscopy

PALM and sptPALM imaging of ParB-mEos2 were performed on a home-built experimental setup based on a Zeiss Axiovert 200 by continuously acquiring 7000 (20000 for sptPALM) images at 50ms exposure time (8ms for sptPALM) with a 561 nm readout laser (Sapphire 561LP, 100mW, Coherent) and continuous illumination with a 405 nm laser for photoactivation (OBIS 40550, Coherent). Data were acquired using custom-made code written in Labview. The readout laser intensity used was 1.4 kW/cm² at the sample plane. The intensity of the 405nm laser was modified during the course of the experiment to maintain the density of activated fluorophores constant while ensuring single molecule imaging conditions. PALM acquisitions were carried out until all mEos2 proteins were photoactivated and bleached. Fluorescent beads (TetraSpeck TM, Life Technologies) were used as fiducial marks to correct for sample drift by post-processing analysis. For cell segmentation, a bright field image was taken on each field of view.

Long-term time-lapse microscopy to monitor of ParB-GFP droplet dynamics was performed on the same optical setup by continuously acquiring images at 50ms exposure

bioRxiv preprint doi: https://doi.org/10.1101/791368; this version posted October 2, 2019. The copyright holder for this preprint (which was not certified by peer review) is the author/funder. All rights reserved. No reuse allowed without permission.

time with a 561 nm readout laser (Sapphire 561LP, 100mW, Coherent) until complete photobleaching.

FRAP experiments on ParB-GFP droplets were conducted on a ZEISS LSM 800 by acquiring 318x318x5 (XYZ) images, every 10 seconds, with 106x106x230 nm^3 voxels exposed during 1.08 µs. Data were acquired using Zen Black (Zeiss acquisition suite). The photo-bleaching of ParB-GFP droplets was performed in circular regions with a diameter of 1.2 µm covering single droplets, in cells with exactly two droplets. To be able to detect them and estimate their intensity afterwards, droplets were only partially photo-bleached (50% approximately). To estimate photo-bleaching during fluorescence recovery, fluorescent intensity was also monitored in bacteria in which ParB-GFP droplets were not pre-bleached. The resulting z-stack images were then projected and analyzed.

ParA degron experiments (DLT3469 strain) were conducted on an Eclipse TI-E/B wide field epifluorescence microscope with a phase contrast objective. To quantify the number of ParB-GFP droplets, samples were prepared at different time points ($t_{induction}$, $t_{induction}$+ 1h, $t_{induction}$ + 2h, $t_{induction}$+ 3h, and one night after induction of degradation) by harvesting cells from the solution, and snapshot images were acquired with an exposure time of 0.6 s. Images were then analysed using the MATLAB-based open-source software MicrobeTracker, and the SpotFinderZ tool (Sliusarenko et al., 2011). To monitor the dynamics of ParB-GFP droplets, images were acquired every 42 seconds.

Data analysis

Localization of single molecules for PALM experiments was performed using 3D-DAOSTORM (Babcock et al., 2012). To discard poorly sampled clusters, localization stitching was used to select clusters with more than 10 ParB-mEos2 molecules. Stitching was

bioRxiv preprint doi: https://doi.org/10.1101/791368; this version posted October 2, 2019. The copyright holder for this preprint (which was not certified by peer review) is the author/funder. All rights reserved. No reuse allowed without permission.

realized by grouping together localizations appearing in successive frames or separated by up to 10 frames (to account for fluorescent blinking) and that were 50 nm apart. Stitched localizations were clustered using a voronoi-based cluster identification method (Cattoni et al., 2017; Levet et al., 2015). In total, 990 clusters with an average of 84 ± 57 localizations (mean $\pm$ std) were analyzed (Figure S1C). To validate that chemical fixation did not alter the localization of ParB droplets, we measured the position droplets in small cells as these most often contained two droplets (Figure S1A). ParB-mEos2 droplets observed by PALM displayed the typical localization pattern of ParB-GFP observed in live cells, i.e. a preferential localization near quarter positions along the cell's main axis (Le Gall et al., 2016). Super-resolved images were reconstructed and classified using our Single-Particle Analysis method (Salas et al., 2017). 990 clusters were sorted into 50 classes (Figure S1D): 51% (506/990) of the total clusters fell into only eight classes (Figure S1E) which were further analysed for particle reconstructions. To measure the size of the partition complex, we reconstructed the three dimensional structures of the eight most represented classes and evaluated their Full-Width at Half Maximum (FWHM, Figure S1F).

Single-molecules for sptPALM analysis were localized using MultipleTarget Tracking (MTT) (Sergé et al., 2008). Single ParB-mEos2 localizations were linked to single tracks if they appeared in consecutive frames within a spatial window of 500nm. To account for fluorescent protein blinking or missed events, fluorescence from single ParB-mEos2 molecules were allowed to disappear for a maximum of 3 frames. Short tracks of less than four detections were discarded from subsequent analysis. The mean-squared displacement (MSD) was computed as described in (Uphoff et al., 2014). The apparent diffusion coefficient was calculated from the MSD using the following equation: $D = MSD / (4\,\Delta t)$, where $\Delta t = 9.7\ msec$. Pairwise distances between ParB molecules were computed as described in

bioRxiv preprint doi: https://doi.org/10.1101/791368; this version posted October 2, 2019. The copyright holder for this preprint (which was not certified by peer review) is the author/funder. All rights reserved. No reuse allowed without permission.

(Stracy et al., 2015). First, the tracks appearing in a spatio-temporal window of 50 nm and 50 frames were linked together to correct for long-time fluorescence blinking of mEos2 that could lead to biased results towards short distances. Then, the distances between the first localizations of each trajectory were computed. Finally, these distances were normalized by a homogeneous distribution obtained from simulating random distributions of 500 emitters in a 1 µm by 0.5 µm nucleoid space.

ParB-GFP droplets from FRAP experiments were tracked using 3D-DAOSTORM (Babcock et al., 2012). The fluorescence intensity of each ParB-GFP droplet was computed by integrating the intensity of a 318nm x 318nm region (3x3 pixels) centered on the centroid of the focus. The trace in Figure 2E was built by averaging the time-dependent fluorescent decay/increase curves from photo-bleached/unbleached ParB-GFP droplets. Each curve was first normalized by the initial droplet intensity, estimated by the average intensity in the three images prior to photo-bleaching. To estimate and correct for natural photo-bleaching, we used bacteria present on the same fields of view, but whose ParB-GFP droplet had not been photo-bleached.

Bacterial strains and plasmids

E. coli strains and plasmids are listed in Tables S1-S2. Cultures were grown at 37°C with aeration in LB (Miller, 1972) containing thymine (10 µg.ml^{-1}) and antibiotics as appropriate: chloramphenicol (10 µg.ml^{-1}); kanamycin (50 µg.ml^{-1}). For microscopy and stability assays, cultures were grown at 30°C with aeration in MGC (M9 minimal medium supplemented with 0.4 % glucose (glycerol or maltose for microscopy assays), 0.2 % casamino acids, 1 mM MgSO4, 0.1 mM CaCl2, 1 µg.ml^{-1} thiamine, 20 µg.ml^{-1} leucine and 40 µg.ml^{-1} thymine).

bioRxiv preprint doi: https://doi.org/10.1101/791368; this version posted October 2, 2019. The copyright holder for this preprint (which was not certified by peer review) is the author/funder. All rights reserved. No reuse allowed without permission.

DLT3298 (*sspB::kan*) was constructed by P1 transduction from strain JW3197 (Baba et al., 2006). The excision of the FRT-kan-FRT selection cassette from strains DLT3053 and DLT3298 was performed using the pCP20 plasmid (Datsenko and Wanner, 2000). The *sspB* gene under the control of the arabinose-inducible P_{BAD} promoter was introduced in DLT3299 by P1 transduction from strain SM997, resulting in DLT3401 (Δ*sspB* P_{BAD}-*sspB kan*). The mini-F pCMD6 carrying $parA_F$-*mVenus*-$ssrA_{AEAS}$ was introduced by transformation in DLT3401 to generate DLT3469. The induction was performed with 0.2% arabinose.

The mini-F plasmids expressing the fluorescently tagged Par proteins are derivatives of the wild-type mini-F pDAG114. The $parB_F$-*mTurquoise2* gene from pJYB240 was introduced into pJYB243 using *Mfe*I and *Spe*I restriction enzymes. A SsrA tag ($SsrA_{AEAS}$; AANDENYSENYAEAS) to specifically induce the degradation of $ParA_F$ was introduced in frame after the last codon of ParA, generating pCMD6. The $ssrA_{AEAS}$ sequence carries the wild-type co-translational signals between $parA_F$ and $parB_F$.

Table S1 : Strains list

(all strains used are derivatives of *E. coli* K12)

DLT1215	*F⁻, thi leu thyA deoB supE rpsL, Δ(ara-leu), zac3051::Tn10*	(Bouet et al., 2006)	
DLT2887	DLT1215 / pJYB212	This work	Figures 1B, 1C, 1D, 2A, 2B, 2C
DLT3053	DLT1215 *Hu-mCherry*, FRT-Kan-FRT	(Le Gall et al., 2016)	
DLT3289	DLT1215 *Hu-mCherry*	This work	
DLT3264	DLT1215 / pJYB216	This work	Figures 3B, 3C, 3D
DLT3298	DLT3289 *sspB::kan*	This work	
DLT3299	DLT3289 Δ*sspB*	This work	

bioRxiv preprint doi: https://doi.org/10.1101/791368; this version posted October 2, 2019. The copyright holder for this preprint (which was not certified by peer review) is the author/funder. All rights reserved. No reuse allowed without permission.

DLT3401	DLT3299 *nocus-P_{BAD}-sspB kan*	This work	
DLT3469	DLT3401 / pCMD6	This work	Figures 4B, 4C, 4D, 4E, 4F
DLT3851	DLT1215 / pJYB213	This work	Figures 2D 2E, 2F, 4A
JW3197	BW25113 *sspB::kan*	Keio collection; (Baba et al., 2006)	
SM997	*sspB::cat, nocus-P_{BAD}-sspB kan*	Gift from C. Lesterlin	

450

Table S2 : Plasmids list

pCMD6	pJYB249, *$parA_F$-mVenus-$ssrA_{AEAS}$ $parB_F$-mTurquoise2*	This work
pDAG114	mini-F, *$repFIA^+$, $ccdB^-$, $resD^+$, $rsfF^+$, cat^+*	(Lemonnier et al., 2000)
pJYB212	pDAG114, *parB-mEos2*	(Sanchez et al., 2015)
pJYB213	pDAG114, *parB-eGfp*	(Sanchez et al., 2015)
pJYB216	pJYB212, Δ*parS*	(Sanchez et al., 2015)
pJYB240	pDAG114, *$parB_F$-mTurquoise2*	J. Rech & J.Y. Bouet, unpublished
pJYB243	pDAG114, *$parA_F$-mVenus*	(Sanchez et al., 2015)
pJYB249	pDAG114, *$parA_F$-mVenus $parB_F$-mTurquoise2*	This work

bioRxiv preprint doi: https://doi.org/10.1101/791368; this version posted October 2, 2019. The copyright holder for this preprint (which was not certified by peer review) is the author/funder. All rights reserved. No reuse allowed without permission.

References

Adachi, S., Hori, K., and Hiraga, S. (2006). Subcellular positioning of F plasmid mediated by dynamic localization of SopA and SopB. J. Mol. Biol. *356*, 850–863.

Ah-Seng, Y., Lopez, F., Pasta, F., Lane, D., and Bouet, J.-Y. (2009). Dual role of DNA in regulating ATP hydrolysis by the SopA partition protein. J. Biol. Chem. *284*, 30067–30075.

Ah-Seng, Y., Rech, J., Lane, D., and Bouet, J.-Y. (2013). Defining the role of ATP hydrolysis in mitotic segregation of bacterial plasmids. PLoS Genet. *9*, e1003956.

Al-Husini, N., Tomares, D.T., Bitar, O., Childers, W.S., and Schrader, J.M. (2018). α-Proteobacterial RNA Degradosomes Assemble Liquid-Liquid Phase-Separated RNP Bodies. Mol. Cell *71*, 1027–1039.e14.

Baba, T., Ara, T., Hasegawa, M., Takai, Y., Okumura, Y., Baba, M., Datsenko, K.A., Tomita, M., Wanner, B.L., and Mori, H. (2006). Construction of Escherichia coli K-12 in-frame, single-gene knockout mutants: the Keio collection. Mol. Syst. Biol. *2*, 2006.0008.

Babcock, H., Sigal, Y.M., and Zhuang, X. (2012). A high-density 3D localization algorithm for stochastic optical reconstruction microscopy. Opt Nanoscopy *1*.

Banani, S.F., Lee, H.O., Hyman, A.A., and Rosen, M.K. (2017). Biomolecular condensates: organizers of cellular biochemistry. Nat. Rev. Mol. Cell Biol. *18*, 285–298.

Baxter, J.C., and Funnell, B.E. (2014). Plasmid Partition Mechanisms. Microbiol Spectr *2*.

Binney, J.J., Dowrick, N.J., Fisher, A.J., and Newman, M.E.J. (1992). The Theory of Critical Phenomena: An Introduction to the Renormalization Group (Oxford University Press).

Bouet, J.-Y., Rech, J., Egloff, S., Biek, D.P., and Lane, D. (2005). Probing plasmid partition with centromere-based incompatibility. Mol. Microbiol. *55*, 511–525.

Bouet, J.-Y., Bouvier, M., and Lane, D. (2006). Concerted action of plasmid maintenance functions: partition complexes create a requirement for dimer resolution. Mol. Microbiol. *62*, 1447–1459.

Bouet, J.-Y., Stouf, M., Lebailly, E., and Cornet, F. (2014). Mechanisms for chromosome segregation. Curr. Opin. Microbiol. *22*, 60–65.

Brangwynne, C.P. (2011). Soft active aggregates: mechanics, dynamics and self-assembly of liquid-like intracellular protein bodies. Soft Matter *7*, 3052–3059.

Brangwynne, C.P., Eckmann, C.R., Courson, D.S., Rybarska, A., Hoege, C., Gharakhani, J., Jülicher, F., and Hyman, A.A. (2009). Germline P granules are liquid droplets that localize by controlled dissolution/condensation. Science *324*, 1729–1732.

Broedersz, C.P., Wang, X., Meir, Y., Loparo, J.J., Rudner, D.Z., and Wingreen, N.S. (2014). Condensation and localization of the partitioning protein ParB on the bacterial chromosome.

bioRxiv preprint doi: https://doi.org/10.1101/791368; this version posted October 2, 2019. The copyright holder for this preprint (which was not certified by peer review) is the author/funder. All rights reserved. No reuse allowed without permission.

Proc. Natl. Acad. Sci. U. S. A. *111*, 8809–8814.

Cattoni, D.I., Cardozo Gizzi, A.M., Georgieva, M., Di Stefano, M., Valeri, A., Chamousset, D., Houbron, C., Déjardin, S., Fiche, J.-B., González, I., et al. (2017). Single-cell absolute contact probability detection reveals chromosomes are organized by multiple low-frequency yet specific interactions. Nat. Commun. *8*, 1753.

Datsenko, K.A., and Wanner, B.L. (2000). One-step inactivation of chromosomal genes in Escherichia coli K-12 using PCR products. Proc. Natl. Acad. Sci. U. S. A. *97*, 6640–6645.

David, G., -C. Walter, J., Broedersz, C.P., Dorignac, J., Geniet, F., Parmeggiani, A., -O. Walliser, N., and Palmeri, J. (2018). Phase separation of polymer-bound particles induced by loop-mediated 1D effective long-range interactions.

Debaugny, R.E., Sanchez, A., Rech, J., Labourdette, D., Dorignac, J., Geniet, F., Palmeri, J., Parmeggiani, A., Boudsocq, F., Anton Leberre, V., et al. (2018). A conserved mechanism drives partition complex assembly on bacterial chromosomes and plasmids. Mol. Syst. Biol. *14*, e8516.

Elowitz, M.B., Surette, M.G., Wolf, P.E., Stock, J.B., and Leibler, S. (1999). Protein mobility in the cytoplasm of Escherichia coli. J. Bacteriol. *181*, 197–203.

Erdmann, N., Petroff, T., and Funnell, B.E. (1999). Intracellular localization of P1 ParB protein depends on ParA and parS. Proc. Natl. Acad. Sci. U. S. A. *96*, 14905–14910.

Faure, L.M., Fiche, J.-B., Espinosa, L., Ducret, A., Anantharaman, V., Luciano, J., Lhospice, S., Islam, S.T., Tréguier, J., Sotes, M., et al. (2016). The mechanism of force transmission at bacterial focal adhesion complexes. Nature.

Fiche, J.-B., Cattoni, D.I., Diekmann, N., Langerak, J.M., Clerte, C., Royer, C.A., Margeat, E., Doan, T., and Nollmann, M. (2013). Recruitment, assembly, and molecular architecture of the SpoIIIE DNA pump revealed by superresolution microscopy. PLoS Biol. *11*, e1001557.

van Gijtenbeek, L.A., Robinson, A., van Oijen, A.M., Poolman, B., and Kok, J. (2016). On the Spatial Organization of mRNA, Plasmids, and Ribosomes in a Bacterial Host Overexpressing Membrane Proteins. PLoS Genet. *12*, e1006523.

Hyman, A.A., Weber, C.A., and Jülicher, F. (2014). Liquid-liquid phase separation in biology. Annu. Rev. Cell Dev. Biol. *30*, 39–58.

Jain, S., Wheeler, J.R., Walters, R.W., Agrawal, A., Barsic, A., and Parker, R. (2016). ATPase-Modulated Stress Granules Contain a Diverse Proteome and Substructure. Cell *164*, 487–498.

Le Gall, A., Cattoni, D.I., Guilhas, B., Mathieu-Demazière, C., Oudjedi, L., Fiche, J.-B., Rech, J., Abrahamsson, S., Murray, H., Bouet, J.-Y., et al. (2016). Bacterial partition complexes segregate within the volume of the nucleoid. Nat. Commun. *7*, 12107.

Lemonnier, M., Bouet, J.Y., Libante, V., and Lane, D. (2000). Disruption of the F plasmid partition complex in vivo by partition protein SopA. Mol. Microbiol. *38*, 493–505.

bioRxiv preprint doi: https://doi.org/10.1101/791368; this version posted October 2, 2019. The copyright holder for this preprint (which was not certified by peer review) is the author/funder. All rights reserved. No reuse allowed without permission.

Levet, F., Hosy, E., Kechkar, A., Butler, C., Beghin, A., Choquet, D., and Sibarita, J.-B. (2015). SR-Tesseler: a method to segment and quantify localization-based super-resolution microscopy data. Nat. Methods *12*, 1065–1071.

Marbouty, M., Le Gall, A., Cattoni, D.I., Cournac, A., Koh, A., Fiche, J.-B., Mozziconacci, J., Murray, H., Koszul, R., and Nollmann, M. (2015). Condensin- and Replication-Mediated Bacterial Chromosome Folding and Origin Condensation Revealed by Hi-C and Super-resolution Imaging. Mol. Cell *59*, 588–602.

McGinness, K.E., Baker, T.A., and Sauer, R.T. (2006). Engineering controllable protein degradation. Mol. Cell *22*, 701–707.

Moffitt, J.R., Pandey, S., Boettiger, A.N., Wang, S., and Zhuang, X. (2016). Spatial organization shapes the turnover of a bacterial transcriptome. Elife *5*.

Monterroso, B., Zorrilla, S., Sobrinos-Sanguino, M., Robles-Ramos, M.A., López-Álvarez, M., Margolin, W., Keating, C.D., and Rivas, G. (2019). Bacterial FtsZ protein forms phase-separated condensates with its nucleoid-associated inhibitor SlmA. EMBO Rep. *20*.

Racki, L.R., Tocheva, E.I., Dieterle, M.G., Sullivan, M.C., Jensen, G.J., and Newman, D.K. (2017). Polyphosphate granule biogenesis is temporally and functionally tied to cell cycle exit during starvation in Pseudomonas aeruginosa. Proc. Natl. Acad. Sci. U. S. A. *114*, E2440–E2449.

Ramamurthi, K.S., and Losick, R. (2009). Negative membrane curvature as a cue for subcellular localization of a bacterial protein. Proc. Natl. Acad. Sci. U. S. A. *106*, 13541–13545.

Rodionov, O., Lobocka, M., and Yarmolinsky, M. (1999). Silencing of genes flanking the P1 plasmid centromere. Science *283*, 546–549.

Salas, D., Le Gall, A., Fiche, J.-B., Valeri, A., Ke, Y., Bron, P., Bellot, G., and Nollmann, M. (2017). Angular reconstitution-based 3D reconstructions of nanomolecular structures from superresolution light-microscopy images. Proc. Natl. Acad. Sci. U. S. A.

Sanamrad, A., Persson, F., Lundius, E.G., Fange, D., Gynnå, A.H., and Elf, J. (2014). Single-particle tracking reveals that free ribosomal subunits are not excluded from the Escherichia coli nucleoid. Proc. Natl. Acad. Sci. U. S. A. *111*, 11413–11418.

Sanchez, A., Rech, J., Gasc, C., and Bouet, J.-Y. (2013). Insight into centromere-binding properties of ParB proteins: a secondary binding motif is essential for bacterial genome maintenance. Nucleic Acids Res. *41*, 3094–3103.

Sanchez, A., Cattoni, D.I., Walter, J.-C., Rech, J., Parmeggiani, A., Nollmann, M., and Bouet, J.-Y. (2015). Stochastic Self-Assembly of ParB Proteins Builds the Bacterial DNA Segregation Apparatus. Cell Syst *1*, 163–173.

Schumacher, M.A., and Funnell, B.E. (2005). Structures of ParB bound to DNA reveal mechanism of partition complex formation. Nature *438*, 516–519.

Schumacher, M.A., Tonthat, N.K., Lee, J., Rodriguez-Castañeda, F.A., Chinnam, N.B.,

bioRxiv preprint doi: https://doi.org/10.1101/791368; this version posted October 2, 2019. The copyright holder for this preprint (which was not certified by peer review) is the author/funder. All rights reserved. No reuse allowed without permission.

Kalliomaa-Sanford, A.K., Ng, I.W., Barge, M.T., Shaw, P.L.R., and Barillà, D. (2015). Structures of archaeal DNA segregation machinery reveal bacterial and eukaryotic linkages. Science *349*, 1120–1124.

Sengupta, M., Nielsen, H.J., Youngren, B., and Austin, S. (2010). P1 plasmid segregation: accurate redistribution by dynamic plasmid pairing and separation. J. Bacteriol. *192*, 1175–1183.

Sergé, A., Bertaux, N., Rigneault, H., and Marguet, D. (2008). Dynamic multiple-target tracing to probe spatiotemporal cartography of cell membranes. Nat. Methods *5*, 687–694.

Shapiro, L., McAdams, H.H., and Losick, R. (2009). Why and how bacteria localize proteins. Science *326*, 1225–1228.

Shin, Y., and Brangwynne, C.P. (2017). Liquid phase condensation in cell physiology and disease. Science *357*.

Stracy, M., Lesterlin, C., Garza de Leon, F., Uphoff, S., Zawadzki, P., and Kapanidis, A.N. (2015). Live-cell superresolution microscopy reveals the organization of RNA polymerase in the bacterial nucleoid. Proc. Natl. Acad. Sci. U. S. A. *112*, E4390–E4399.

Strom, A.R., Emelyanov, A.V., Mir, M., Fyodorov, D.V., Darzacq, X., and Karpen, G.H. (2017). Phase separation drives heterochromatin domain formation. Nature *547*, 241–245.

Surovtsev, I.V., and Jacobs-Wagner, C. (2018). Subcellular Organization: A Critical Feature of Bacterial Cell Replication. Cell *172*, 1271–1293.

Taylor, J.A., Pastrana, C.L., Butterer, A., Pernstich, C., Gwynn, E.J., Sobott, F., Moreno-Herrero, F., and Dillingham, M.S. (2015). Specific and non-specific interactions of ParB with DNA: implications for chromosome segregation. Nucleic Acids Res.

Toro, E., and Shapiro, L. (2010). Bacterial chromosome organization and segregation. Cold Spring Harb. Perspect. Biol. *2*, a000349.

Uphoff, S., Sherratt, D.J., and Kapanidis, A.N. (2014). Visualizing protein-DNA interactions in live bacterial cells using photoactivated single-molecule tracking. J. Vis. Exp.

Visser, B.J., Joshi, M.C., and Bates, D. (2017). Multilocus Imaging of the E. coli Chromosome by Fluorescent In Situ Hybridization. Methods Mol. Biol. *1624*, 213–226.

Walter, J.C., and Barkema, G.T. (2015). An introduction to Monte Carlo methods. Physica A: Statistical Mechanics and Its Applications.

Zwicker, D., Decker, M., Jaensch, S., Hyman, A.A., and Jülicher, F. (2014). Centrosomes are autocatalytic droplets of pericentriolar material organized by centrioles. Proc. Natl. Acad. Sci. U. S. A. *111*, E2636–E2645.

Zwicker, D., Hyman, A.A., and Jülicher, F. (2015). Suppression of Ostwald ripening in active emulsions. Phys. Rev. E Stat. Nonlin. Soft Matter Phys. *92*, 012317.

Zwicker, D., Seyboldt, R., Weber, C.A., Hyman, A.A., and Jülicher, F. (2016). Growth and

bioRxiv preprint doi: https://doi.org/10.1101/791368; this version posted October 2, 2019. The copyright holder for this preprint (which was not certified by peer review) is the author/funder. All rights reserved. No reuse allowed without permission.

division of active droplets provides a model for protocells. Nat. Phys. *13*, 408.

bioRxiv preprint doi: https://doi.org/10.1101/791368; this version posted October 2, 2019. The copyright holder for this preprint (which was not certified by peer review) is the author/funder. All rights reserved. No reuse allowed without permission.

Figures

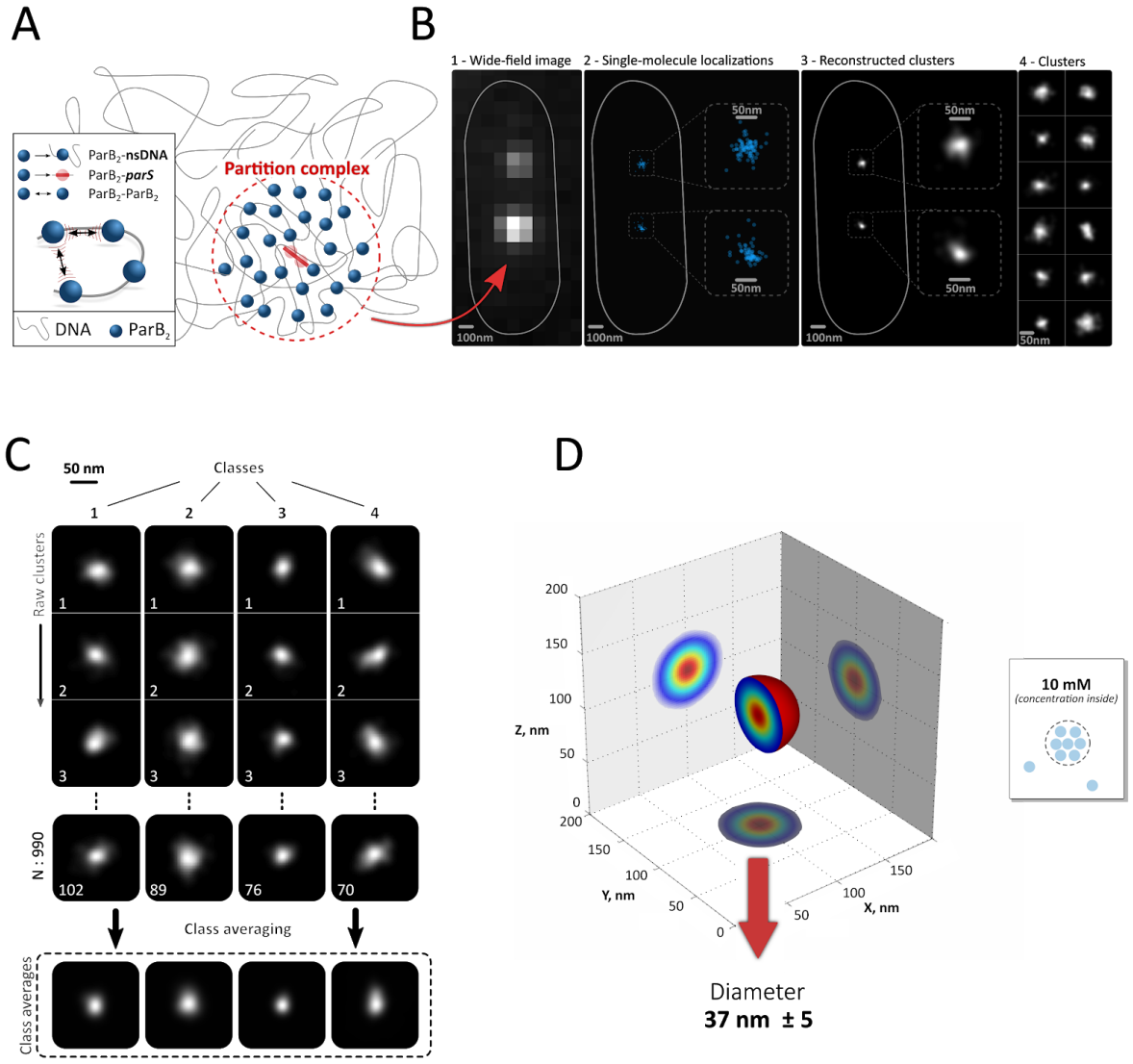

Figure 1. ParB is confined into spherical nano-condensates. (A) Schematic representation of a ParB partition complex (red circle). ParB is represented by blue spheres, the centromeric *parS* sequence by a red line, and non-specific DNA (plasmid and bacterial chromosome) is represented by a grey curved line. Three types of interactions have been reported: ParB-*parS* (high affinity, 2 nM), ParB-non-specific DNA (low affinity, 0.3-0.5 µM), and ParB-ParB dimer (low affinity, 0.3-1 µM) (Ah-Seng et al., 2009; Sanchez et al., 2015; Taylor et al., 2015). **(B)** Partition complexes (n=990) were visualized by either widefield microscopy (first panel) or by PALM (second and third panels for raw localizations and reconstruction representations, respectively). Magnified views of the two partition complexes are shown for clarity (panel 3). Panel 4 displays representative ParB partition complex reconstructions from other cells to exemplify the heterogeneity in shapes. **(C)** Super-resolved images of ParB partition complexes were classified using single-particle analysis to overcome heterogeneity between single complexes. ParB complexes of the most populated classes exhibited spherical shapes. **(D)** A three-dimensional reconstruction of the ParB partition complex was obtained using the most populated classes. Diameter was estimated by calculating the full width at half maximum. Right panel: schematic representation of the ParB partition complex and estimation of ParB concentration based on the size of the complex and the number of ParB molecules measured experimentally (see Results). Measurements were performed in different biological replicates.

bioRxiv preprint doi: https://doi.org/10.1101/791368; this version posted October 2, 2019. The copyright holder for this preprint (which was not certified by peer review) is the author/funder. All rights reserved. No reuse allowed without permission.

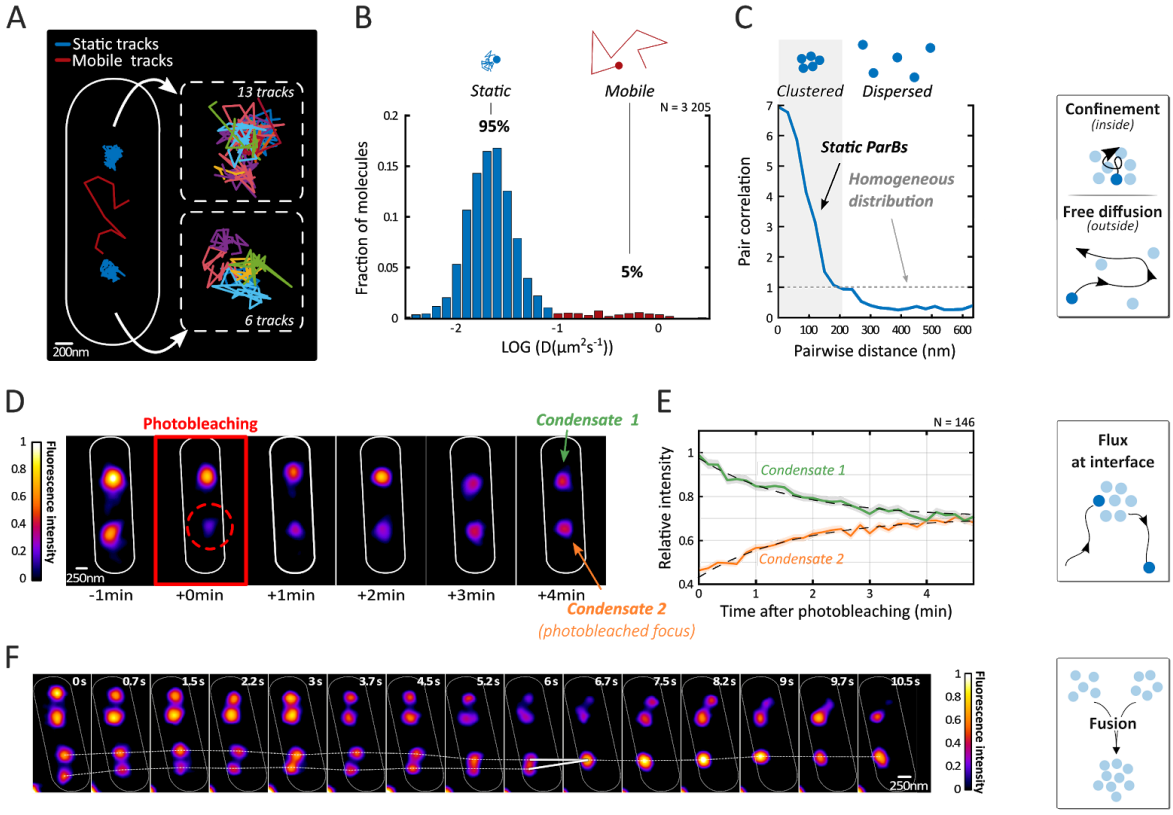

Figure 2. Dynamic properties of ParB condensates. (A) Representative image of a live cell (white contour) and trajectories of single ParB molecules (static: blue; mobile: red). Right panels show magnified views of each ParB condensate with different static trajectories shown with different colors. **(B)** Histogram of apparent diffusion coefficients for static (blue) and mobile (red) trajectories. The precision of localization is indicated with a vertical dashed line. n=156 (number of cells). **(C)** Pairwise distance analysis of static trajectories. Expectation for a homogeneous distribution is shown as a horizontal dashed line. Right panels: schematic representations of ParB proteins within (top) and outside (bottom) ParB condensates. n=156 (number of cells). **(D)** Representative example of a Fluorescence Recovery After Photobleaching experiment. A single ParB-GFP condensate (red circle) was photobleached in a cell containing two condensates. **(E)** The average intensity of photobleached ParB condensates (orange) increased over time with a concomitant and symmetric decrease in the fluorescence intensity of the unbleached condensate (green). This requires single ParB proteins to exchange between liquid and gas-like phases (right panel). Grayed shade represents standard error of the mean. Dashed lines represent the behavior predicted from modeling in Figure S2. n=146 (number of cells). **(F)** Representative example of a fast time-lapse fluorescence movie. Four ParB condensates can be seen to fluctuate and fuse during the movie (white line). Schematic representation of a fusion event is shown in the right panel. Measurements were performed in different biological replicates (n>14).

bioRxiv preprint doi: https://doi.org/10.1101/791368; this version posted October 2, 2019. The copyright holder for this preprint (which was not certified by peer review) is the author/funder. All rights reserved. No reuse allowed without permission.

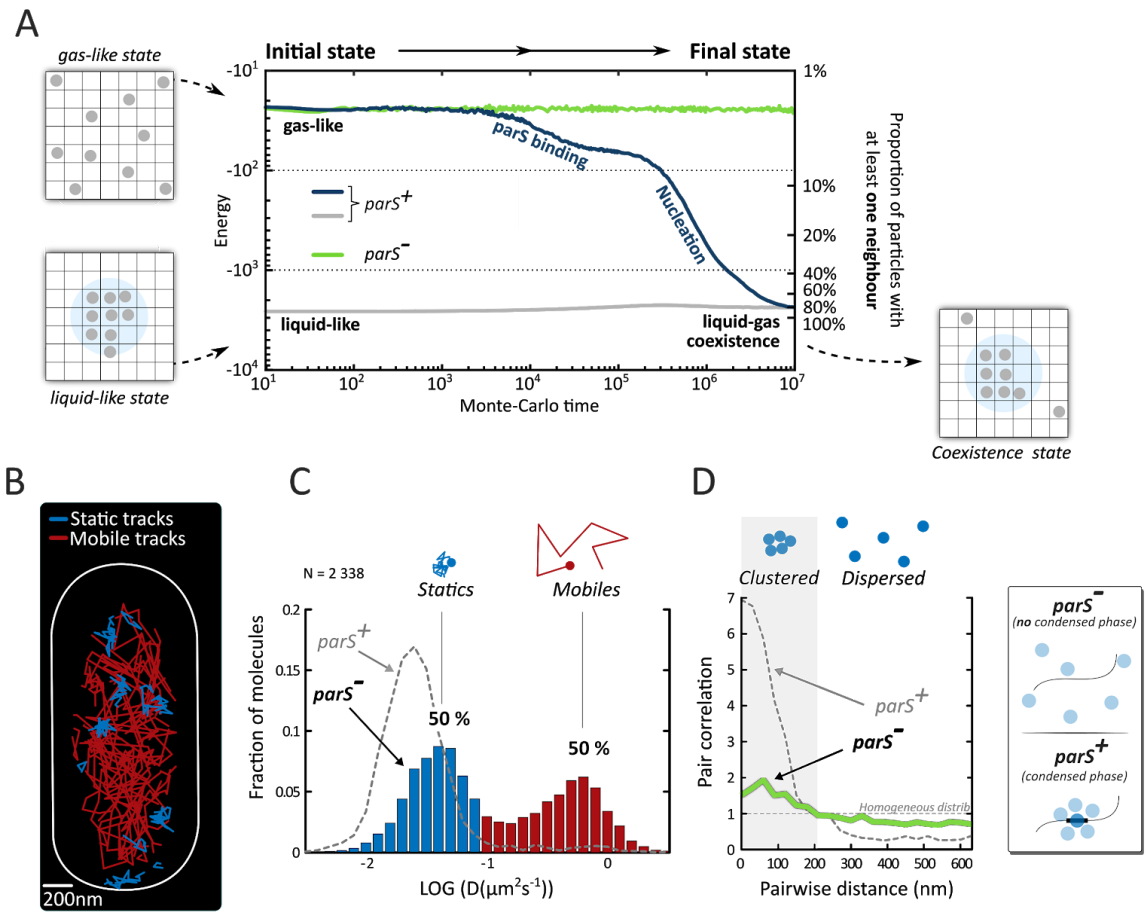

Figure 3. Centromeric sequences, and ParB-ParB interactions are required for the nucleation and stability of ParB condensates. **(A)** The movement of three hundred ParB proteins within a simulated cell was governed by free diffusion (1 µm²/s), weak ParB-ParB dimer interactions (J=4.5 kT) and high-affinity ParB-*parS* interactions. Regardless of initial conditions, ParB proteins formed a condensate in the presence of *parS10* (gray, blue). In contrast, no condensate is formed in the absence of a nucleation sequence (green). Schematic representations are used to show the initial and final configurations (left and right panels). For simplicity, parS+ refers to a simulation with *parS10*. **(B)** Representative single-molecule tracking experiment of ParB in absence of *parS*. Static trajectories are shown in blue and mobile trajectories in red. **(C)** Distribution of apparent diffusion coefficients for static (blue, 50%) and mobile trajectories (red, 50%). The distribution for a wild-type strain containing *parS* (same data as in Figure 2B) is shown as a dashed grey line for comparison. n=209 (number of cells). **(D)** Pairwise distance analysis of static trajectories in absence of *parS* (green curve). The expected curve for a homogeneous distribution is shown as a horizontal dashed line. The distribution for a wild-type strain containing *parS* is shown as a dashed grey line for comparison (same data as in Figure 2C). Schematic representations of single-molecule ParB trajectories in the absence (top) and presence of *parS* (bottom) are shown in the panels on the right. n=209 (number of cells). Measurements were performed in different biological replicates.

bioRxiv preprint doi: https://doi.org/10.1101/791368; this version posted October 2, 2019. The copyright holder for this preprint (which was not certified by peer review) is the author/funder. All rights reserved. No reuse allowed without permission.

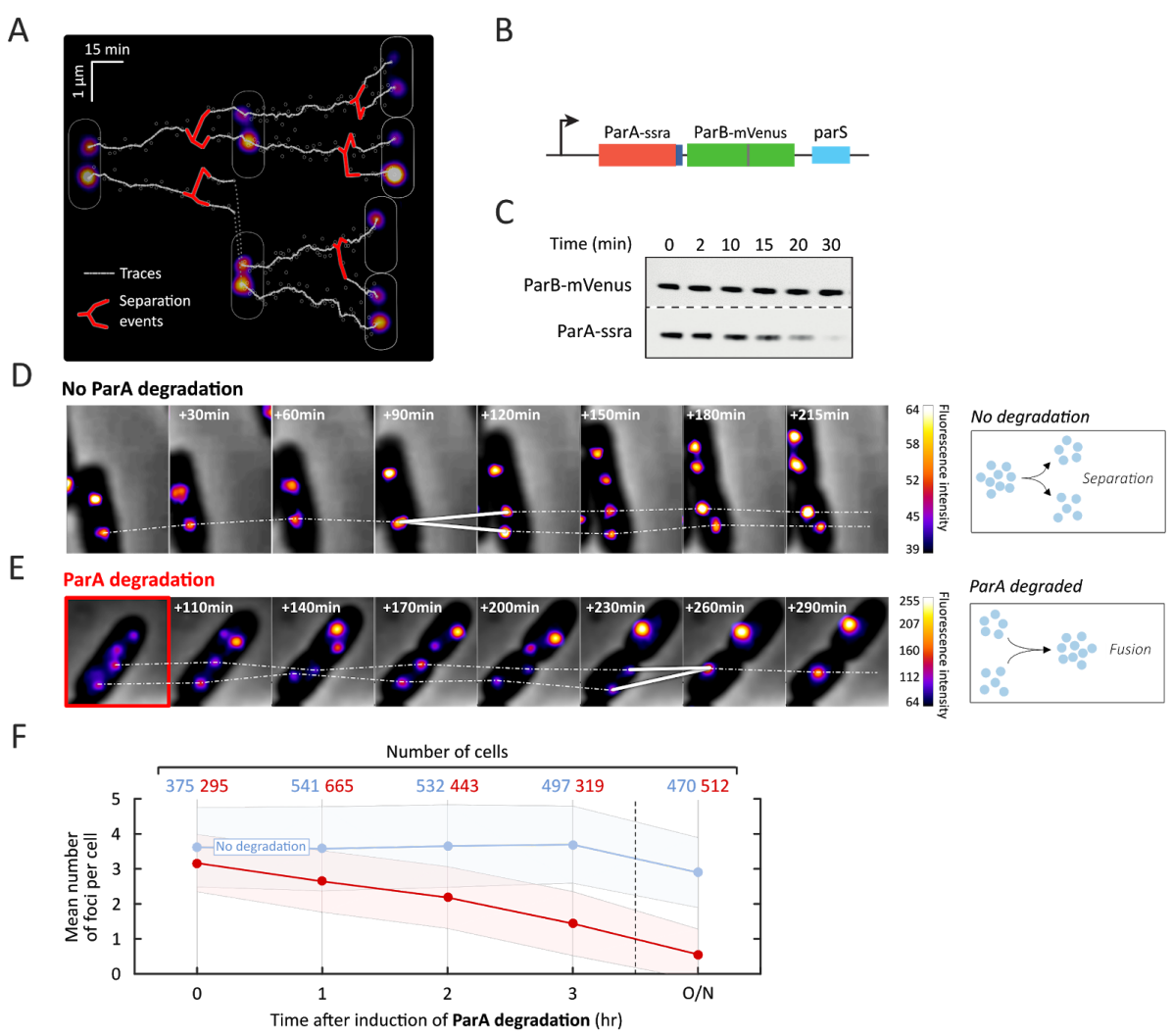

Figure 4. The ParA ATPase is required for ParB condensates to remain stably separated during cell-cycle times. (A) Representative kymograph displaying the trajectories of ParB condensates over cell-cycle times (white lines). Splitting of condensates are shown by red forks. The fluorescence images of ParB condensates at three different times as well as the cell outlines are shown for simplicity. **(B)** Genetic construct used for the targeted degradation of ParA. **(C)** Time course Western blot of ParA and ParB upon induction of ParA-ssra degradation. **(D)** Representative time lapse experiment of a ParA-ssra strain without induction of ParA degradation. Trajectories of ParB condensates (white dashed line) and a splitting event (white fork) are shown. Scalebar represents fluorescence intensity. Right panel: schematic representation of a splitting event in the presence of ParA. **(E)** Representative time lapse experiment of a ParA-ssrA strain upon induction of ParA-ssra degradation. Dashed lines represent the trajectories of two ParB condensates. A fork displays a fusion event between two ParB condensates. Right panel: schematic representation of this process. **(F)** Quantification of the average number of ParB condensates per cell in a ParA-ssra strain with (red circles) or without (blue circles) ParA degradation. The induction of ParA degradation was initiated at time 0. Shaded areas represent standard deviation. Note that the slight decrease in foci number (~20%) without ParA degradation after overnight (O/N) culture corresponds to the decrease in cell length (~20%) (see Figure S4). Numbers of cells are shown above plot. Measurements were performed in different biological replicates.

bioRxiv preprint doi: https://doi.org/10.1101/791368; this version posted October 2, 2019. The copyright holder for this preprint (which was not certified by peer review) is the author/funder. All rights reserved. No reuse allowed without permission.

Supplementary Figures

Figure S1

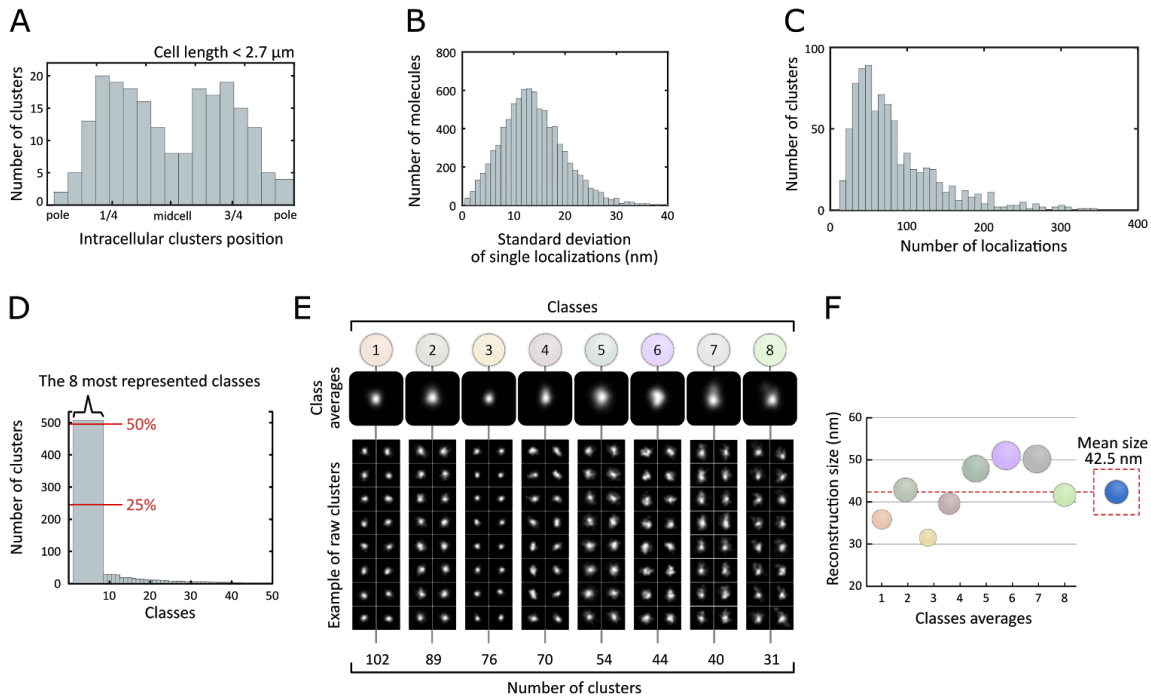

S1A To control for fixation artifacts, we built the histogram of localization of ParB clusters along the main axis of the cell. ParB clusters in fixed cells were localized near the quarter positions of the cell axis, mirroring the localization pattern of partition complexes from live experiments (Le Gall et al., 2016). Only clusters of small cells with a length of less than 2.7 µm were selected to avoid cells with more than 2 ParB complexes that would confound the overall localization pattern. n=990 (number of clusters).

S1B Histogram of the standard deviations of the localization positions from single molecules. The mean of the standard deviation of localization, which provides an estimate of the localization precision, is $14 \pm 6\ nm$ (mean ± std). n=990 (number of clusters).

S1C Histogram of single ParB-mEos2 localizations per cluster. The average number of localizations per cluster is 84 ± 57 (mean ± std). n=990 (number of clusters).

S1E Examples of raw clusters for the eight most represented classes, which represent more than 50% of the total number of clusters (n=990).

S1F Full width at half maxima (reconstruction size) extracted from the 3D reconstructions obtained from each class average. The average reconstruction size is $42.5\ nm \pm 6.9$ (mean ± std).

bioRxiv preprint doi: https://doi.org/10.1101/791368; this version posted October 2, 2019. The copyright holder for this preprint (which was not certified by peer review) is the author/funder. All rights reserved. No reuse allowed without permission.

Figure S2

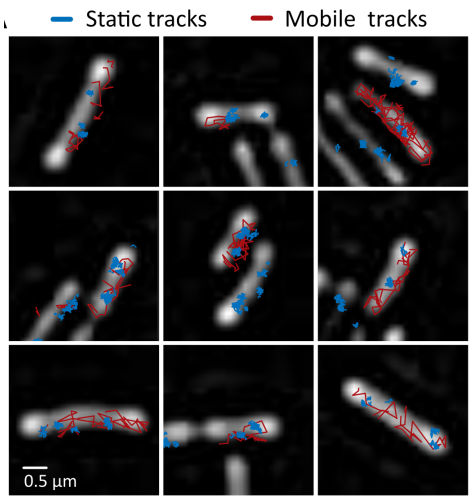

S2A Representative images of live cells and trajectories of single ParB molecules (static: blue; mobile: red). Static trajectories tend to clusterize while mobile trajectories display a dispersed nucleoid localization.

Calculation of residence time in ParB condensates

In Figure 2E are shown the fluorescence intensity profiles in time from both ParB condensates after the photo-bleaching of the condensate that we number by 1. We first notice that the foci intensity curves are symmetric (see Figure S2B below) by doing a simple manipulation of the data : $I_1^*(t) = 2I_\infty - I_1(t)$ is the symmetric curve of I_1 according to the asymptotic intensity value $I_\infty = I_1(t \to \infty) = I_2(t \to \infty) \simeq 0.7$.

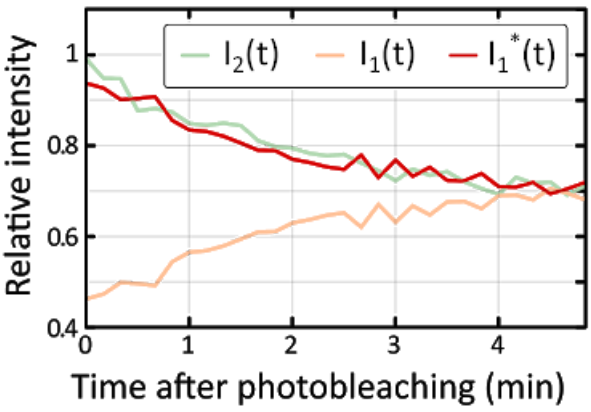

S2B *Fluorescence intensity curves of photo-bleached (orange, $I_1(t)$) and unbleached condensates (green, $I_2(t)$). The $I_1^*(t)$ curve (red) is symmetric to $I_1(t)$ according to the asymptotic value $I_\infty = I_1(t \to \infty) = I_2(t \to \infty) \simeq 0.7$. It shows the symmetrical behavior between both condensates which we used in the model developed here.*

bioRxiv preprint doi: https://doi.org/10.1101/791368; this version posted October 2, 2019. The copyright holder for this preprint (which was not certified by peer review) is the author/funder. All rights reserved. No reuse allowed without permission.

We therefore describe the FRAP experiments by the following simple kinetic model on the distribution of ParB proteins in both condensates and the rest of the cytoplasm.

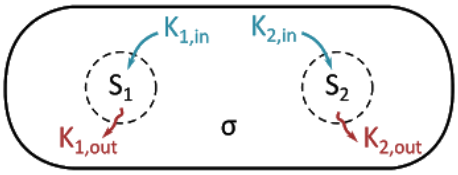

S2C *Schematic representation of the model parameters.* $S_1(t)$ *(* $S_2(t)$*, respectively) is the ratio of the average number of fluorescent ParB-GFP proteins in the photo-bleached (un-bleached, resp.) condensate.* $\sigma(t)$ *is the ratio of the average number of fluorescent ParB-GFP proteins outside of the condensates. Due to symmetry, we consider :* $k_{1,in} = k_{2,in} = k_{in}$ *and* $k_{1,out} = k_{2,out} = k_{out}$.

This model is described by the following equations

$$\frac{dS_1(t)}{dt} = k_{1,in}\sigma - k_{1,out}S_1(t)$$

$$\frac{d\sigma(t)}{dt} = -(k_{1,in} + k_{2,in})\sigma(t) + k_{1,out}S_1(t) + k_{2,out}S_2(t) \qquad (1)$$

$$\frac{dS_2(t)}{dt} = k_{2,in}\sigma(t) - k_{2,out}S_2(t)$$

where $S_1(t)$ and $S_2(t)$ are, respectively, the ratios of average number of ParB proteins in the condensates (droplets) F_1 and F_2 after photobleaching and σ(t) the ratio of average number of ParB proteins in the cytoplasm after photobleaching. All these quantities were normalized by $S_2(0)$ (see also below) in order to directly compare the experimental normalized intensities $I_1(t)$ and $I_2(t)$ with the model variables $S_1(t)$ and $S_2(t)$. Rates $k_{i,in}$ ($k_{i,out}$, resp.) ($i = 1, 2$) count for the probability per unit of time to enter (exit, resp.) the condensate F_i . Note that here we assume that the fluorescence intensity is proportional to the number of ParB proteins, and that there are no steric/exclusion effects among ParB.

Due to the symmetric behavior of the FRAP signals for each condensate (Figure S2B), we assume that the kinetic rates are the same for each condensate F_i. Therefore the equations write:

$$\frac{dS_1(t)}{dt} = k_{in}\sigma(t) - k_{out}S_1(t)$$

bioRxiv preprint doi: https://doi.org/10.1101/791368; this version posted October 2, 2019. The copyright holder for this preprint (which was not certified by peer review) is the author/funder. All rights reserved. No reuse allowed without permission.

$$\frac{d\sigma(t)}{dt} = -2k_{in}\sigma(t) + k_{out}(S_1(t) + S_2(t)) \qquad (2)$$
$$\frac{dS_2(t)}{dt} = k_{in}\sigma(t) - k_{out}S_2(t)$$

Starting from these assumptions, we first study the asymptotic limit of eq. 2 where we notice from Figure S2B that $S_1(t \to \infty) = S_2(t \to \infty) = S_\infty \simeq 0.7$. In this case it is simple to notice that :

$$\frac{S_\infty}{\sigma_\infty} = \frac{k_{in}}{k_{out}} \qquad (3)$$

Live data provided an estimation of this ratio (Figure 2B): $S_\infty/\sigma_\infty = k_{in}/k_{out} \simeq 4.5$.
We then write the explicit time dependence of $S_1(t)$, $S_2(t)$ and $\sigma(t)$. As intensities have been normalized by the natural photo-bleaching, we can first use the conservation of the total number of proteins just after FRAP photobleaching:

$$S_1(0) + S_2(0) + \sigma(0) = S_1(t) + S_2(t) + \sigma(t) = S_{tot} \qquad (4)$$

It is useful to consider that the same condition is valid all over the acquisition (i.e. we also assume that degradation of ParB is negligible during the 5min-experiment), therefore at long times:

$$S_{1,\infty} + S_{2,\infty} + \sigma_\infty = \left(2 + \frac{k_{out}}{k_{in}}\right) S_\infty = S_{tot}. \qquad (5)$$

The conservation of the total particle number (ratio) in eq. 4 allows us to eliminate the equation on the variable σ from the equations 2 and write the new set of equations :

$$\frac{dS_1(t)}{dt} = k_{in}S_{tot} - (k_{in} + k_{out})S_1(t) - k_{in}S_2(t)$$
$$\frac{dS_2(t)}{dt} = k_{in}S_{tot} - (k_{in} + k_{out})S_2(t) - k_{in}S_1(t) \qquad (6)$$

General solutions of the systems of equations (6) is as follows:

$$S_1(t) = S_\infty - \left[\left(S_\infty - \frac{1}{2}S_+(0)\right)e^{-2k_{in}t} + \frac{1}{2}S_-(0)\right]e^{-k_{out}t}$$
$$S_2(t) = S_\infty - \left[\left(S_\infty - \frac{1}{2}S_+(0)\right)e^{-2k_{in}t} - \frac{1}{2}S_-(0)\right]e^{-k_{out}t} \qquad (7)$$

where equations (6) are still symmetrical for the 1 ↔ 2 exchange. To perform a fit of the date, it is useful to consider the symmetric and antisymmetric variables $S_\pm(t) = S_1(t) \pm S_2(t)$ and write :

bioRxiv preprint doi: https://doi.org/10.1101/791368; this version posted October 2, 2019. The copyright holder for this preprint (which was not certified by peer review) is the author/funder. All rights reserved. No reuse allowed without permission.

$$\frac{dS_-(t)}{dt} = -k_{out}S_-(t)$$
$$\frac{dS_+}{dt} = 2k_{in}S_{tot} - (2k_{in} + k_{out})S_+(t) \qquad (8)$$

The first equation (8) (in accordance with solutions in eq. 7) gives the simple exponential solution:

$$S_-(t) = S_-(0)e^{-k_{out}t} \qquad (9)$$

A simple exponential fit (see Figure S2D below) already provides :

$$k_{out} = (0.0100 \pm 0.0004)\ s^{-1}$$

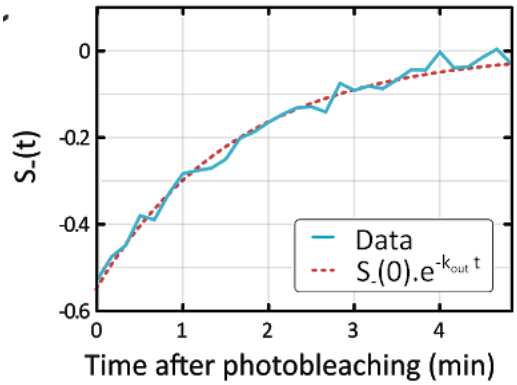

S2D *Anti-symmetric intensity curve* $S_-(t) = S_1(t) - S_2(t)$ *(blue) and associated fitted curve* $S_-(t) = S_-(0)\, e^{-k_{out}t}$ *(red).*

or, reciprocally, a residence time in the focus:

$$\tau_{out} = 1/k_{out} \simeq 100s$$

and

$$S_-(0) = (-0.540 \pm 0.022)$$

By using the knowledge of the previously estimated parameters, k_{out} and $S_-(t)$, one can still exploit the solution of $S_2(t)$ (in eq. 7) to fit the remaining parameters k_{in} and $S_+(t)$. We fitted the data with the right side of the following rewritten equation (see fit in Figure S2E):

$$(S_2(t) - S_\infty)e^{k_{out}t} = -\left[\left(S_\infty - \frac{1}{2}S_+(0)\right)e^{-2k_{in}t} - \frac{1}{2}S_-(0)\right] \qquad (10)$$

bioRxiv preprint doi: https://doi.org/10.1101/791368; this version posted October 2, 2019. The copyright holder for this preprint (which was not certified by peer review) is the author/funder. All rights reserved. No reuse allowed without permission.

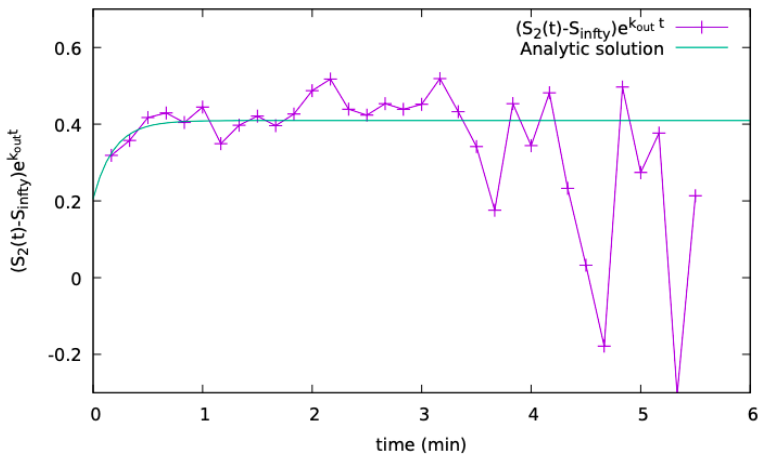

S2E *Intensity curve* $(S_2(t) - S_\infty(t))e^{k_{out}t}$ *(purple) and associated fitted curve (see eq. 10)(cyan).*

From this fit, we obtain $k_{in} = (0.044 \pm 0.012)\ s^{-1}$ and $S_+(0) = 0.97 \pm 0.18$. The reciprocal of k_{in} represents the residence time of ParB in the cytoplasm:

$$\tau_{in} = \sim 23\ s$$

Remarkably, from this analysis and by using equation 3, we find a ratio of rates:

$$\frac{k_{in}}{k_{out}} = (4.4 \pm 1.3)$$

which provides an estimate (~90%) of the proportion of ParB proteins confined within ParB condensates, in good agreement with experimental results (~95%). The agreement between theoretical and experimental curves can be verified by plotting eqs. (7) together with the experimental datasets (Figure 2E).

bioRxiv preprint doi: https://doi.org/10.1101/791368; this version posted October 2, 2019. The copyright holder for this preprint (which was not certified by peer review) is the author/funder. All rights reserved. No reuse allowed without permission.

Figure S3

The Lattice-Gas model

The ParB proteins in the nucleoid were modeled by a Lattice Gas (LG), which is the paradigmatic system of particles displaying attractive contact interactions (Binney et al., 1992). It is important to note that the LG model presents a first-order phase transition between a gas phase, in which the particles diffuse homogeneously throughout the lattice, and a liquid-gas coexistence phase, in which liquid droplets coexist with diffusing particles in the gas phase. An exchange of particles between the two phases maintains a dynamic equilibrium. As we will see below, the metastable region of the gas can account for the experimental observations on ParBS. We use the LG as a qualitative model for ParB in the nucleoid in order to offer a proof of concept of the mechanism of formation of the ParBS complexes.

For 1d, 2d square, and 3d simple cubic lattices, the LG coordination number is *q = 2d*. Recent work (David et al., 2018) shows that a 1D LG model on a fluctuating polymer like DNA can undergo phase separation and that such a model can, after averaging over the polymer conformational fluctuations, be assimilated approximately to a LG with short range (nearest-neighbor) interactions on a lattice with an effective, perhaps fractal, coordination number between 2 and 6 (G. David, PhD Thesis, in preparation). The increase in coordination number from the value of 2 expected for a linear polymer is due to the combined effects of nearest-neighbor (spreading) interactions along the polymer and bridging interactions between proteins widely separated on the polymer, but close in space. Here for simplicity and purposes of illustration of the basic mechanism we adopt a simple cubic (sc) lattice $(q_{\mathrm{sc}} = 6)$.

The ParB proteins were modeled by particles with a diameter $a = 5\,nm$, which were located on the nodes of a simple cubic lattice representing segments of the nucleoid on which ParB is able to bind to or unbind from. The distance between nearest-neighbour sites was as large as the size of a particle, i.e. $5\,nm$. The lattice was chosen to display the dimension of a bacterial nucleoid: $L_x = L_y = 0.5\,\mu m$ and $L_z = 2\,\mu m$ (equivalent to $L_x = L_y = 100\,a$ and $L_z = 400\,a$). The total number of binding sites in the lattice was then $N_s = 4.10^6$. To match the experimentally determined number of ParB proteins per condensate, the particle number was fixed at 300. Thus, the particle density $\rho = N/N_s$ was very low ($\rho \sim 10^{-4}$), placing the LG model in a configuration where only a first-order phase separation transition can occur. Particles could interact between each other when they are at adjacent sites on the sc lattice (nearest neighbour contact interaction) with a magnitude J. For the LG model, the total energy ε of the system is: $\varepsilon = -J \sum_{<i,j>} \phi_i \phi_j$, where ϕ_i is the

bioRxiv preprint doi: https://doi.org/10.1101/791368; this version posted October 2, 2019. The copyright holder for this preprint (which was not certified by peer review) is the author/funder. All rights reserved. No reuse allowed without permission.

occupation variable at site i taking the value 1 if the site i is occupied or 0 if not. The sum Σ runs over the pairs of nearest-neighbour sites <i,j> of the lattice.

The phase diagram of the LG model

The sc LG model displays only 3 parameters: the particle density ρ, the temperature T (or equivalently β) and the coupling J between particles. Despite its minimalism aspect, the LG model is a paradigmatic model for phase transitions and displays a rich phase diagram (Binney et al., 1992). The metastable region is bound by the coexistence and the spinodal curves, where the LG can transiently remain in a metastable gas or liquid state before crossing a free energy barrier to reach a stable coexistence state. The time required to cross this free energy barrier can be very long, but their transition rate can also be considerably increased by a nucleation factor such as a *parS* site, the effect of which can be modeled within the LG model by particles fixed on the lattice by a strong binding potential. The phenomenology observed in the metastable region is the same as that observed experimentally for a ParB condensate: without a *parS* site, ParBs were homogeneously distributed in the cell, while with *parS* sites, we observed formation of ParB droplets. The *parS* sites catalyzed the condensation of ParB droplets.

Before presenting MC simulations for a finite size system representing the DNA in the bacterial volume, it is instructive to present the thermodynamics of liquid-gas phase separation (infinite volume limit). Although no analytical solution exists for the sc LG with nearest-neighbour interactions, mean field theory provides an approximate analytical solution that gives a global perspective. For a fixed value of J, the coexistence and spinodal curves are usually presented in the density-temperature plane (ρ, T). In the present case it is more useful to fix the temperature at its room value, T_r, then plot the coexistence and spinodal curves in the (ρ, J) plane, with J measured in units of the thermal energy, $k_B T_r$. The mean field phase diagram is presented in Fig. S3A. For the LG model we note the exact (particle-hole) symmetry about the critical density $\rho_c = 1/2$, where the coexistence and spinodal curves coincide.

bioRxiv preprint doi: https://doi.org/10.1101/791368; this version posted October 2, 2019. The copyright holder for this preprint (which was not certified by peer review) is the author/funder. All rights reserved. No reuse allowed without permission.

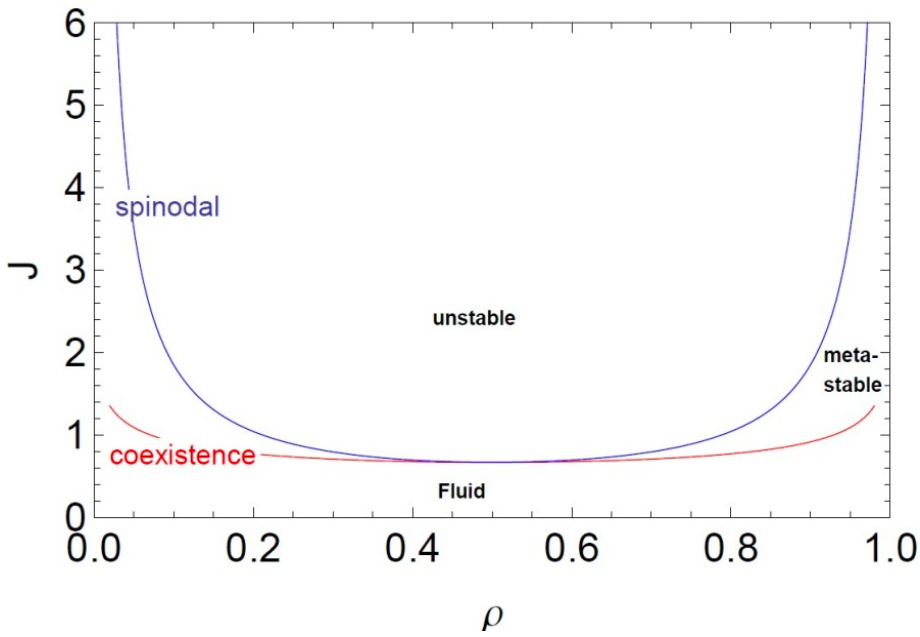

***Fig. S3A**. The mean field coexistence and spinodal curves are presented in the density-coupling plane (ρ, J) with the homogeneous fluid, metastable, and unstable regions indicated.*

At biological density $\rho \sim 10^{-4}$ and room temperature, the homogeneous (possibly meta or unstable) system is in the extreme low-density regime. Although the mean field prediction for the coexistence curve is asymptotically exact in this regime, the same is not true for the mean field spinodal curve. In this limit it is possible, however, to perform an asymptotically exact low density (virial) expansion that leads to a simple expression for the system free energy from which the pressure and chemical potential can be obtained. The coexistence curve is found by equating the pressure and chemical potential in the gas and liquid phases which are in equilibrium. The spinodal curve is determined by the divergence of the isothermal compressibility. At low density $\rho \ll 1$ the gas branch coexistence (coex) and spinodal (sp) curves are given by (G. David, in preparation, 2019):

$$J_{\text{coex}}(\rho) \approx -\frac{2\ln(\rho)}{q_{\text{sc}}}$$

$$J_{\text{sp}}(\rho) \approx -\ln\left(q_{\text{sc}}\rho\right)$$

We present in Fig. S3B the asymptotically exact low-density results for the coexistence and spinodal curves in the density-coupling plane (*ρ*, *J*). The above limiting low density forms indicate that the coexistence and spinodal curves become straight lines in a log-linear plot.

bioRxiv preprint doi: https://doi.org/10.1101/791368; this version posted October 2, 2019. The copyright holder for this preprint (which was not certified by peer review) is the author/funder. All rights reserved. No reuse allowed without permission.

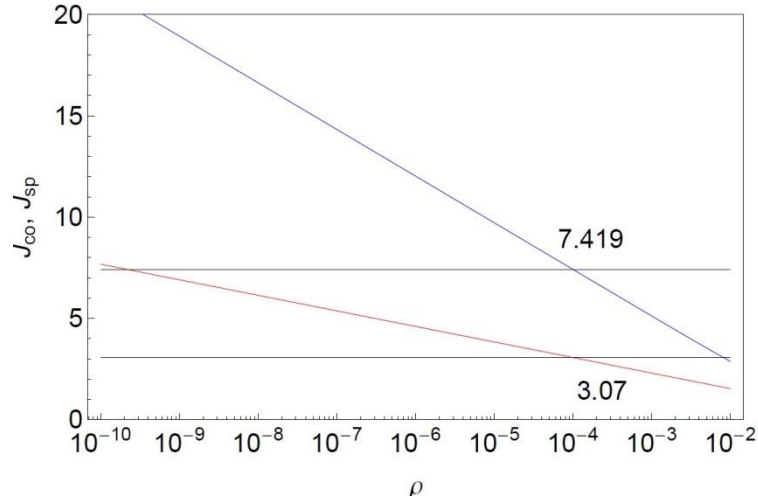

***Fig. S3B**. The asymptotically exact low-density results for the coexistence (red) and spinodal (blue) curves in the density-coupling plane (ρ, J). The upper and lower limits of metastability in J (black horizontal lines) at $\rho = 10^{-4}$ are shown ($J_{low} = 3.07$, $J_{up} = 7.42$). The homogeneous fluid phase is stable below the coexistence curve, metastable between the coexistence and spinodal curves, and unstable above the spinodal curve.*

A system prepared above the coexistence curve will at equilibrium show phase separation between a low density gas phase with $\rho_{\text{coex}}^{\text{gas}}(J) = e^{-\frac{1}{2}q_{sc}J}$ and a high density liquid phase with (by particle-hole symmetry) $\rho_{\text{coex}}^{\text{liq}}(J) = 1 - \rho_{\text{coex}}^{\text{gas}}(J)$. If the system is prepared in a metastable gas state the time needed to nucleate the phase transition depends on the distance from the coexistence and spinodal curves since the nucleation barrier decreases as the spinodal curve is approached, where it vanishes.

We performed Monte Carlo simulations of the LG in contact with a thermal bath using the standard Metropolis algorithm (Walter and Barkema, 2015). In the following, $\beta = 1/(k_b T)$ is the inverse of thermal energy, where T is the absolute temperature and k_b the Boltzmann constant (in the following, all energies are expressed in units of the thermal energy $k_b T$, thus $\beta = 1$). The Monte Carlo procedure corresponding to a unit time step is the following:

1. Choose a particle at random,
2. Propose a move to a random empty site of the lattice.
3. Calculate the energy difference $\Delta\epsilon = \varepsilon_f - \varepsilon_0$ between the initial and final state,
4. If $\Delta\epsilon < 0$, the displacement is accepted, otherwise the displacement is accepted with a probability $P = e^{-\beta\Delta\epsilon}$,
5. Return N times to step 1.

bioRxiv preprint doi: https://doi.org/10.1101/791368; this version posted October 2, 2019. The copyright holder for this preprint (which was not certified by peer review) is the author/funder. All rights reserved. No reuse allowed without permission.

The particle relocation of the step 2 defines the order of the time unit of the Monte Carlo simulation as approximately one second : ParB proteins diffusing at $D \sim 1\ \mu m^2.s^{-1}$ (Figure 2B) can move at any point on a $1\ \mu m^2$ nucleoid after one second.

We first used simulations to estimate the range of the interaction term J for which the LG model is found in the metastable region, i.e. between the coexistence and the spinodal lines (see Figure S3B and S3C below). To find these lines and define a J, we calculated the energy of the system at equilibrium as a function of J with increasing and decreasing variations. Thus, the signature of the first-order transition was visible with a hysteresis cycle and the range of J for which the LG was metastable was bound by the two jumps of energy: the jump at low J corresponding to the coexistence curve and the jump at large J corresponding to the distance from the spinodal curve at which the nucleation time in the presence of a free energy barrier becomes comparable to the simulation time.

To identify the hysteresis cycle, we increased and decreased J by steps of $\Delta J = 0.005$. After incrementing J by ΔJ (or $-\Delta J$ depending on initial conditions), the system was first thermalized to the new coupling value. The sampling of the energy was subsequently performed at intervals long enough to consider that the sampling was not correlated. After 8.10^4 independent samplings, J was increased to its new value.

We observed different regimes (see Figure S3C below):

I. In the case of a weak initial J, the system was first in a gas phase (the interactions are too weak to maintain a cohesive phase). In such a configuration, the system favors a homogeneous distribution of particles to maximize entropy with very few interactions between the particles. Then, by crossing the coexistence line, the gas state became metastable but the system remained in that state until it reached the point before the spinodal line where nucleation time became comparable to the simulation one and the gas phase was depleted in favour of the liquid-gas coexistence phase.

II. In the case of a high initial J, the system was first in the liquid-gas coexistence phase: the particles condensed locally in a droplet and increased the number of nearest-neighbour interactions. The droplet coexisted with a small fraction of freely diffusing particles. Then, by approaching and then crossing the coexistence line, the system switched smoothly to a gaseous phase state. This protocol defines a hysteresis cycle determined by simulations for a finite system that delimits the value of J for which the LG is effectively in the metastable phase. Because of the protocol this range depends on the time scale of the simulations. We note furthermore that fluctuations in finite size systems are more important than in an infinite one (thermodynamic limit) and therefore the range of effective metastability determined by simulations should lie within the true thermodynamic range, as is the case.

bioRxiv preprint doi: https://doi.org/10.1101/791368; this version posted October 2, 2019. The copyright holder for this preprint (which was not certified by peer review) is the author/funder. All rights reserved. No reuse allowed without permission.

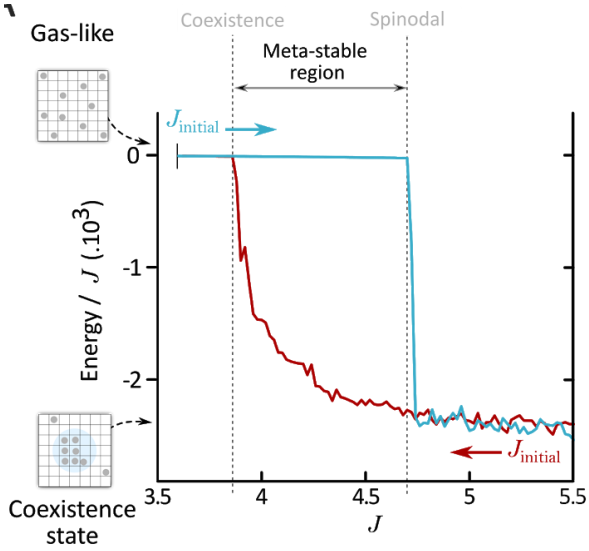

S3C *Variation of the energy at the equilibrium of the Lattice-Gas model according to the magnitude of the interaction between particles (J), in the presence of parS. For weak J 's, the system is in the gaseous state, while for high J 's, the system is in the liquid state. The transition from one state to another takes place in a metastable region delimited by coexistence and spinodal lines. In this region, the state of the system depends on the initial state, either gaseous (blue curve) or liquid (red curve). We observed a hysteresis cycle which is characteristic of a first-order phase transition of the LG model between the two states. For the simulations shown on Figure 3A, we used J =4.5.*

The coupling range for setting the LG in the metastable regime was estimated as $3.9 < J < 4.7$. This range falls, as it should, in the thermodynamic range $(3.07 < J < 7.42)$ computed above (see Fig. S3B). In the dynamic simulations of the main text, we chose the value $J = 4.5$ close to the estimated upper limit in order to be as close as possible to the experimental value of 90% of ParB inside the droplets ((Sanchez et al., 2015), and here). This value is in semi-quantitative agreement with other simulation works on ParB-ParB (Broedersz et al., 2014; David et al., 2018). At $J = 4.5$ the gas density on the thermodynamic coexistence curve is very low $\rho_{coex}^{gas} \approx 10^{-6}$ (see Fig. S3A) and the liquid density very close to 1, which leads to 98% of ParB inside the droplets. We expect, however, simulations on finite size systems to show quantitative differences with respect to the thermodynamic limit because of boundary effects and enhanced fluctuations.

<u>Effect of *parS* on the nucleation</u>

The LG provides a proof of concept of the physical mechanisms at work in the formation of ParB droplets: in the metastable region of the liquid-gas coexistence phase, the nucleation factor *parS* site catalyzes the formation of a ParB droplet. To show this effect, we first thermalized the system from a random distribution of ParB on the nucleoid (corresponding to the absence of coupling, i.e. $J = 0$) to the coupling of the simulation $J = 4.5$. At time $t = 0$, we monitored the time evolution of ε and the number of ParB in

bioRxiv preprint doi: https://doi.org/10.1101/791368; this version posted October 2, 2019. The copyright holder for this preprint (which was not certified by peer review) is the author/funder. All rights reserved. No reuse allowed without permission.

the droplet (Figure 3A). The parameters were the same as before, and we averaged over 250 different thermal histories.

We checked two different conditions: **(i)** without a *parS* sequence; **(ii)** with a *parS* sequence, which were modeled by 10 lattice sites with high affinity for ParB proteins (in practice, 10 ParB were always fixed on these sites after a short transitional time). As a control, we also performed a simulation **(iii)** with an initial start where all the particles packed in a single droplet centered on a *parS* sequence. Convergence towards the equilibrium state was achieved in this case by simple relaxation and not by nucleation.

The gas phase is characterized by small values of the energy $\varepsilon \sim 0$ (the particles are dispersed in the lattice) while in the liquid-gas coexistence phase, the condensation of the particles increases the number of interactions, and therefore the energy $\varepsilon << 0$.

In the case **(i)** without *parS*, the system remained at a small equilibrium value $\varepsilon \approx -24.10^3$ until the final moment of the simulations $t_f = 3.10^7 MC\ steps$, i.e., the condensation into droplet was not observed. In the case **(ii)**, the system was initially at the small value of $\varepsilon = -24.10^3$ as in case (i), but was followed by another plateau between $t = 10^4$ and $10^5 MC\ steps$ corresponding to the binding of ParB to the 10 *parS* sites. The energy decreased from $\varepsilon \approx -24$ to -80.10^3, which corresponds to the interactions between the ten ParB fixed side by side on the parS. At the time $t \sim 3.10^5 MC\ steps$, the system switched from a high energy value to a low value, corresponding to the formation of a droplet around *parS*. At larger time $t > 3.10^5 MC\ steps$, the signal saturated at $\varepsilon \sim -2650.10^3$, indicating that the droplet is stable. Thus, the addition of *parS* reduced the nucleation time by at least two orders of magnitude. These observations correspond to experimental phenomenology: without *parS*, ParB is homogeneously distributed throughout the cell, whereas with *parS*, ParB forms protein condensates.

Case **(iii)** is the control simulation with the fully packed droplet. It took, at large times, the same value of ε as case **(ii)** after a slight decrease corresponding to the escape from the cluster of particles in the gas phase coexisting with the droplet. We also monitored the number of particles inside the droplet (Figure 3A). We observed ~80% of the particles in the droplet, which is in semi-quantitative agreement with experiments (~90% in (Sanchez et al., 2015), and 95% from Figure 2B). In conclusion, the ParB complex behaves similarly to a system in the metastable region of the liquid-gas coexistence phase (Figure S3A). The addition of *parS* acting as nucleator for ParB condensation significantly reduces the time it takes to form a ParB droplet.

To assess the effect of interaction strengths of ParB particles on their nucleation, we performed additional simulations with lower or higher values of J for our two initial conditions (a gas-like and liquid-like state). When the system was first in a gas phase with weak interaction strengths (J = 3.5 kT, Figure S3D), particles were unable to form condensates regardless of the presence of *parS* sites. Without *parS* sites, particles favored a homogeneous distribution while in presence of *parS* sites particles equilibrated to a state with only ParB particles bound specifically to the centromeric sequence. In the initial conditions where ParB particles were released from a liquid-like state, the system

bioRxiv preprint doi: https://doi.org/10.1101/791368; this version posted October 2, 2019. The copyright holder for this preprint (which was not certified by peer review) is the author/funder. All rights reserved. No reuse allowed without permission.

equilibrated to a final state where we did not observe nucleation but rather ParB particles specifically bound to the centromeric sequence.

In the case of strong interaction strengths (J = 6 kT, Figure S3E), with or without *parS* sites, particles initially in a gas-like state immediately started forming small droplets (hence low energy values at initial conditions) until a single large droplet prevailed over the others. In presence of centromeric sequences, no binding of ParB to *parS* was visible due to the fast local aggregation of ParBs at short timescales giving rise to energy variations of the same order of magnitude. In the case where ParB particles were released from a liquid-like state, particles remained in this state throughout the simulation timescales used here. Overall, these simulations highlight the range of interaction strengths required for ParB to nucleate specifically at *parS*. For weak ParB-ParB interactions (low J), ParB particles are unable to form a condensate, regardless of the presence of centromeric sequences. For strong ParB-ParB interactions (high J), ParB particles nucleate spontaneously independently of the presence of *parS* sequences and therefore of the plasmid to segregate. A balance of ParB-ParB interactions strengths and the presence of the centromeric sequence are therefore both essential for the partition complex to form and to function in plasmid partitioning.

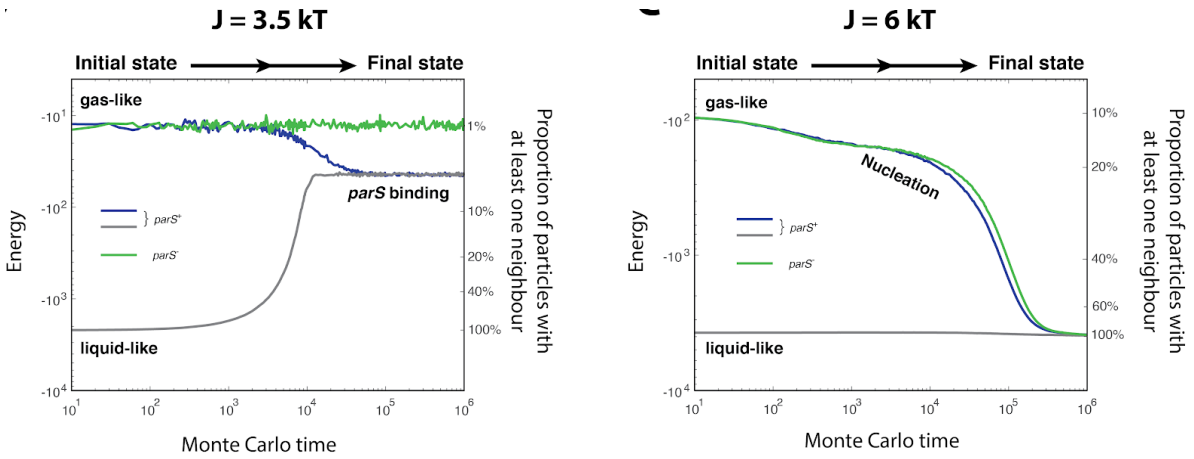

S3D-E Monte-Carlo simulations of the Lattice-Gas model for weak (left panel) and strong (right panel) interaction strengths between ParB particles. (D) *Weak ParB-ParB interactions (J=3.5 kT) and high-affinity ParB-parS interactions are here considered. Regardless of initial conditions (gas or liquid-like state), ParB proteins are unable to form a condensate in the presence of parS10 (gray, blue) and the system equilibrates to a state where only ParBs bind specifically to the centromeric sequences.* ***(E)*** *In contrast, when strong ParB-ParB interactions (J=6 kT) are considered, small droplets immediately appear and nucleate into a single larger condensate independently of the presence or absence of a nucleation sequence (blue and green curves, respectively).*

bioRxiv preprint doi: https://doi.org/10.1101/791368; this version posted October 2, 2019. The copyright holder for this preprint (which was not certified by peer review) is the author/funder. All rights reserved. No reuse allowed without permission.

Figure S4

A

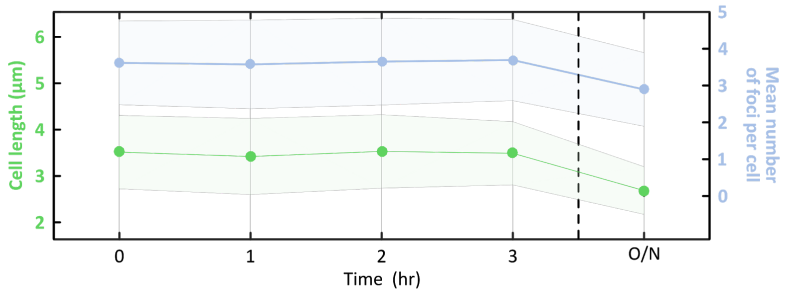

S4A Average cell length and average number of ParB condensates per cell during time-lapse imaging of the ParA-ssrA strain (pCMD6/DLT3469), without induction of ParA degradation. The decrease in the average number of foci per cell observed after one night is due to a change in cellular metabolism, as reflected by the decrease in the average cell length, presumably due to entrance into stationary phase. Shaded areas represent standard deviation.